UCLouvain

AGRO LOUVAIN

Faculté des bioingénieurs

NAP-XPS analysis in a heterogeneous catalysis context

Auteur : Sacha Duriau

Promoteur(s) : Pr. Damien Debecker, Ir. Pierre Eloy

Lecteur(s) : Pr. Eric Gaigneaux, Pr. Arnaud Delcorte

Année académique 2024-2025

Mémoire de fin d'études présenté en vue de l'obtention du diplôme de Bioingénieur : Chimie et Bio-industries

Acknowledgement

I would like to begin by expressing my warm thanks to all those who supported and accompanied me throughout this master's thesis.

First and foremost, I am sincerely grateful to Pierre Eloy, whose pedagogical guidance was essential throughout this project. His precise and patient answers, his ability to explain clearly the principles and operation of the new NAP-XPS system, and his attentive supervision were invaluable. Despite occasional misunderstandings and results that did not always meet expectations, his support enabled me to move forward and overcome the challenges I faced. His guidance has made a significant contribution to the completion of this work.

I would also like to thank Professor Damien Debecker for accepting to supervise this thesis despite his already full schedule. I am truly appreciative of the time he dedicated to following my progress. His advice and ideas were extremely valuable in shaping and advancing this project.

My sincere thanks go to Giovanni Pampararo, who synthesized the catalysts used in this study and was always available to answer my questions. His responsiveness and willingness to help were greatly appreciated.

I am also thankful to Professors Eric Gaigneaux and Arnaud Delcorte for agreeing to serve on the jury of this dissertation.

A warm thank you goes to Léo Philippe, my fellow NAP-XPS partner throughout this journey. Our mutual support and collaboration were a real asset.

Finally, I would like to thank my parents, for their unwavering support and encouragement over the years, as well as for financing my studies. My deep thanks also go to Charles, Ruis, and Arthur, aka Joachim, with whom I shared all my lunch breaks this year—always in a great mood. And of course, thank you to my amazing group of friends, "PAP", without whom these years of study would have been far less fun.

FRS-FNRS is acknowledged for having allowed the acquisition of the NAP-XPS instrument via the project GEQ-UG01822F.

The FSR (UCLouvain) is also acknowledged for having completed the funding, as the technological platform SUCH of IMCN.

Abstract

Since catalytic reactions in heterogeneous catalysis occur at the surface, understanding surface structure and composition is essential. Near-Ambient Pressure X-ray Photoelectron Spectroscopy is a powerful technique that enables the investigation of catalytic surfaces under conditions close to those of real operation. This master's thesis presents an initial study using the newly installed NAP-XPS system at UCLouvain. As a preliminary step, a pure copper plate was analyzed under various gas atmospheres and temperatures. This allowed us to evaluate the performance of the system and to better understand key instrumental parameters. Additionally, we aimed to evaluate the extent of electron loss occurring in the gas phase. In a second time mesoporous Cu/SiO_2 catalyst was studied to explore the migration of copper species to the surface during calcination. Although this objective was not fully achieved, this work provided valuable insights into gas-phase charge compensation, fluidic effect under the cone, and factors influencing signal attenuation from gas-phase.

Table of Contents

Contents

Table of Abbreviation

XPS: X-ray Photoelectron Spectroscopy

SEM: Scanning Electron Microscopy

TEM: Transmission Electron Microscopy

TOF-SIMS: Time of Flight Secondary Ion Mass Spectroscopy

DRIFT: Diffuse Reflectance Infrared Fourier Transform

NAP-XPS: Near Ambient Pressure X-ray Photoelectron Spectroscopy

IMFP: Inelastic Mean Free Path

UHV: Ultra High Vacuum

RWGS: Reverse Water Gas Shift

AASG: Aerosol Assisted Sol Gel

XRD: X Ray Diffraction

AdC: Adventitious Carbon

FWHM: Full Width Half Max

RSF: Relative Sensitivity Factor

ECC: Environmental Charge Compensation

Table of Figures

1. Introduction

Heterogeneous catalysis is everywhere, from refining fuels and producing fertilizers to cleaning car exhausts and synthesizing everyday chemicals. It plays a central role in countless industrial and environmental processes, making it one of the most essential pillars of modern chemistry. In heterogeneous catalysis, the surface of the catalyst plays a crucial role, as it is the site where reactants are adsorbed, activated, and converted into products[1]. Understanding the surface structure, composition, and chemical state is therefore essential for unravelling reaction mechanisms and optimizing catalytic performance. To achieve this, various surface characterization techniques can be used, such as SEM, TEM, TOF-SIMS, DRIFT or N_2 physisorption[2]. In this work, we will focus on X-ray Photoelectron Spectroscopy (XPS), and more specifically on Near-Ambient Pressure XPS (NAP-XPS), which allows the investigation of catalyst surfaces under conditions closer to realistic reaction environments.

This master thesis focuses on the newly installed NAP-XPS instrument at UCLouvain and its potential for studying heterogeneous catalysis. As this is a brand-new and highly sensitive tool, it is essential to first understand how the instrument responds under various conditions. Several adjustments and preliminary tests are therefore required before reliable analysis can be performed on actual catalyst. To this end, we began with a simple model system — a copper plate — to evaluate the instrument's behaviour and optimize measurement conditions. Once this groundwork was laid, we moved on to a more complex and catalytically relevant material: a Cu–SiO_2 catalyst, that was designed to perform the non-oxidative ethanol dehydrogenation into acetaldehyde[3].

1.1. Basic Principles of XPS

To understand the complete story, the basic principles and limitations of conventional XPS will first be explained.

1.1.1. Photoelectric effect

The story of x-ray photoelectron spectroscopy (XPS) began with the discovery of the photoelectric effect by Heinrich Hertz in 1887. He notes that when a surface is irradiated with ultraviolet light, electrons are ejected. This discovery was explained in 1905 by Albert Einstein. He showed that light behaves like a stream of localized energy quanta, known as light quanta or photons[4]. Equation 1 [5] describes the photoionization process. When a photon with energy

$h\nu$ (where h is Planck's constant and ν is the frequency of the light) interacts with an atom or molecule A, it can transfer all its energy to one electron. If this energy is high enough, the electron is ejected from A, resulting in a positively charged ion A^+. The asterisk (*) indicates that the ion may be left in an excited state. The remaining energy from the photon becomes the kinetic energy of the emitted electron[6].

$$A + h\nu \rightarrow A^{*+} + e^- \quad (1)$$

Photoemission from X-rays was first observed by Robinson and Rawlinson in 1914[4]. However, the development of the instrument as we know it today began in the second half of the 20th century. The first use of photoemission as an analytical method was introduced by Steinhardt and Serfass in 1951[7]. Most of the progress in developing the technique was made by Kai Siegbahn and his team at the University of Uppsala in Sweden, during the 1950s and 1960s[8].

When X-rays with sufficient energy strike a sample, their energy is first used to overcome the binding energy of a core-level electron, allowing its release from the atom. The excess energy is then transferred to the emitted electron as kinetic energy. This kinetic energy E_k is measured by an electron energy analyzer. Their binding energy E_b can be easily determined by rearranging Equation 2 [9]. The spectrometer work function ϕ_w is the energy offset between the vacuum level of the sample and the vacuum level of the electron energy analyzer in an XPS system. It represents the minimum energy required for a photoemitted electron to enter the spectrometer and be detected[9].

$$E_k = h\nu - E_b - \phi_w \quad (2)$$

The binding energies of electrons differ for each subshell of every element, resulting in a unique pattern of peaks in XPS at specific binding energies that can be used to identify the element. Photoelectron peaks are labelled by the element and its orbital, e.g., "O 1s" for electrons from the 1s orbital of oxygen, in Figure 1. The binding energy of an electron is an intrinsic property of the material and the specific orbital it occupies and it does not depend on the X-ray source used[10]. In XPS, all elements, except hydrogen and helium [11] can be detected, as they possess core electrons [9].

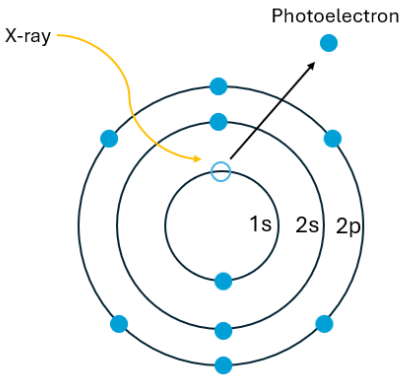

Figure 1 : Schematic of photoelectron generation from 1s orbital after X-ray irradiation

1.1.2. Spin-orbit coupling

For orbitals with non-zero orbital angular momentum (l > 0, meaning non-s orbitals), spin–orbit coupling causes the spectral line to split into a doublet. This happens because the electron's spin can align either parallel or antiparallel to the magnetic field generated by its orbital motion. As a result, two distinct total angular momentum states, j, are formed through the interaction between the spin and orbital angular momenta, according to Equation 3, where s is the spin angular momentum quantum number (± ½)[6].

$$J = l + s \tag{3}$$

The area ratio of the doublets can be easily predicted by Equation 4.

$$area\ ratio = ratio\ of\ \ 2j + 1\ values \tag{4}$$

In this thesis, the focus will be on copper (Cu). An electron in the p orbital of a Cu atom, where the orbital angular momentum quantum number is l = 1, can have two possible total angular momentum values: j = 1/2 and j = 3/2. As a result, the Cu 2p signal in XPS appears as a doublet with a peak area ratio of 1:2 distant from 19.8 eV as shown on Figure 2a.

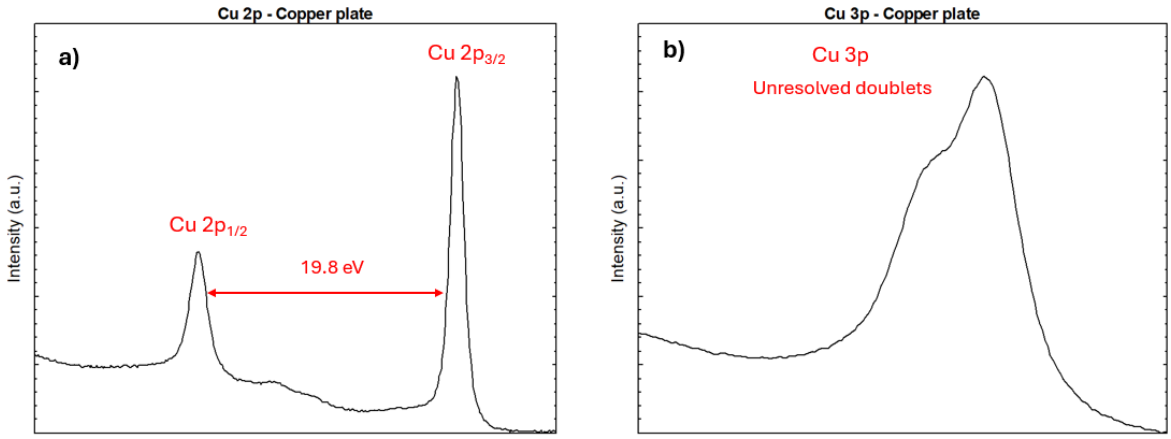

Figure 2 : a) Cu 2p doublets from a copper plate. b) Unresolved Cu 3p doublets from a copper plate.

The energy difference between the two peaks, caused by spin–orbit coupling, increases with the atomic number Z when comparing elements within the same subshell. However, for a given principal quantum number n, this energy difference tends to decrease as the orbital angular momentum l increases[12]. This explains why, in the case of the Cu 3p orbital, the spin–orbit splitting between the $3p_{3/2}$ and $3p_{1/2}$ levels is relatively small, typically around 2 to 3 eV. This separation is comparable to the natural linewidth of the peaks, which includes instrumental broadening and lifetime effects. As a result, the two components significantly overlap and appear as a single broad, unresolved peak in the XPS spectrum shown on Figure 2b. Making the doublet difficult or even impossible to distinguish[13].

1.1.3. Auger electrons

The ejection of a core electron creates an electron vacancy. This ionised state is quickly relaxed by filling the vacancy with an electron from a higher-level orbital, generally a valence orbital. Two phenomena can then occur: fluorescence, which will not be discussed here, and the emission of an Auger electron[9].

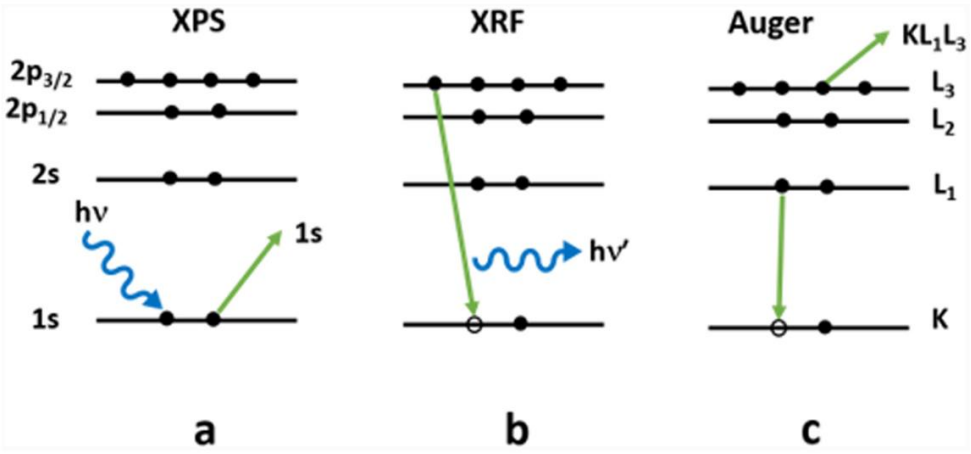

Figure 3 : a) emission of a photoelectron, b) x-ray fluorescence, c) emission of an Auger electron [9]

The emission of an Auger electron involves three electron transitions, which the three letters notation used to describe Auger peaks refer to. For example, the main Auger peak of copper is labelled Cu LMM, which indicates that the initially ejected photoelectron comes from the L orbital, the electron filling the vacancy comes from the M orbital, and the final Auger electron emitted also originates from the M orbital[9].

The kinetic energy of an emitted Auger electron depends on the binding energies of the atomic orbitals involved. The primary beam must have enough energy to ionize a core level (Ew in Figure 4). An electron from a higher energy level, usually near the Fermi level (e.g., transition from level X to W), fills the vacancy, releasing energy. This energy is transferred to a third electron (Ey), which is then ejected. The kinetic energy of the Auger electron equals the difference in binding energies of the three levels involved, minus the sample's work function[14,15].

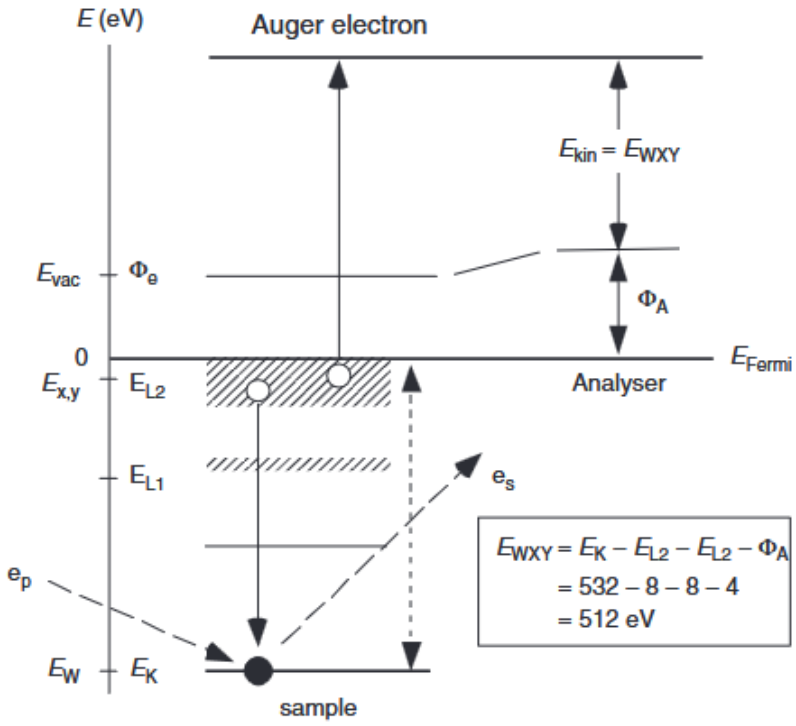

Figure 4 : Example of Auger process for the transition of oxygen KLL [15]

Auger spectroscopy can be particularly useful, as the Cu $2p_{3/2}$ peak of Cu^0 and Cu^+ are very close in binding energy, around 932.6 eV for and 932.4 eV respectively[16], making them difficult to distinguish using photoelectron peak alone. Additionally, both species lack shake-up satellite features, which are characteristic of Cu^{2+}. To differentiate between the Cu^0 and Cu^+ oxidation states, the Cu LMM Auger transition is often used. In this case, the kinetic energy of the Cu LMM peak is typically around 918.6 eV for Cu^0 and approximately 916.8 eV for Cu^+ [16].

1.1.4. Chemical environment

One reason XPS is so valuable is its ability to reveal the chemical environment of atoms in a sample, including their nearest neighbours and oxidation state. Both factors influence not only the exact binding energy of the photoelectron peaks but also their shape[9]. These alterations are known as chemical shifts. In Figure 5, the C 1s peak is correctly positioned at 284.8 eV, which corresponds to the expected binding energy of carbon. The spectrum also displays several additional components at higher binding energies, indicating the presence of different chemical environments. These features are consistent with adventitious carbon (AdC) contamination on the Cu surface. The peak is deconvoluted into four components, each

representing a distinct chemical state of carbon. The most intense contribution, centred at 284.7 eV, is attributed to aliphatic carbon (C–(C,H)), typically originating from airborne hydrocarbons, organic solvents, or general exposure to volatile organic compounds in ambient air. In addition to this dominant peak, several minor components reveal more oxidized forms of carbon. A peak at 286.2 eV corresponds to C–OH and C-O-C bonds, commonly associated with alcohol or ether groups. At 287.7 eV, a component appears that is related to carbonyl functionalities such as ketones, or aldehydes. Finally, the peak at 288.9 eV can be assigned to O–C=O species, pointing to the presence of carboxylic acids, ester or carbonate-like structures[17,18].

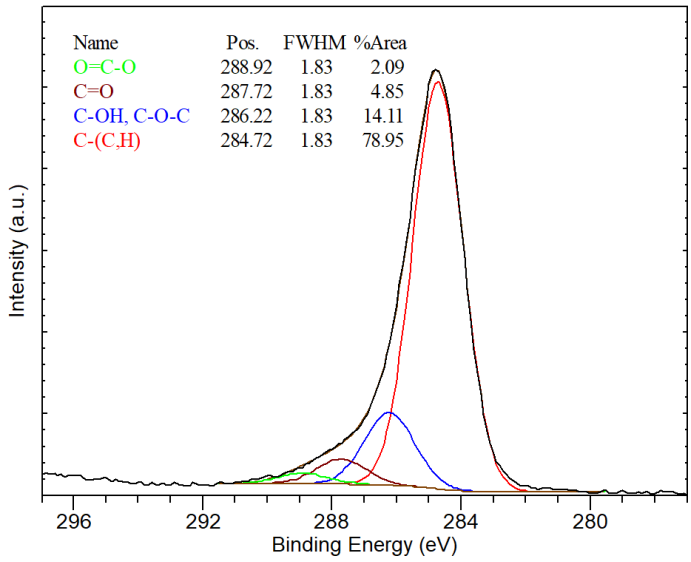

Figure 5 : C 1s peak with 4 components from Cu plate typical from contamination Carbon

1.1.5. Shake – up structure

Figure 6 shows additional features on the Cu 2p region at higher binding energies, known as shake-up peaks. These occur after photoionization, there is a certain probability that the ion will remain in an excited state a few eV above the ground state, due to interaction with the outgoing photoelectron[6]. When this happens, the emitted photoelectron loses some kinetic energy, resulting in a peak shifted to a higher binding energy than the main photoelectron line[19]. Shake-up structures are only observed in the Cu^{2+} oxidation state. They are absent in Cu^{0} and Cu^{+} compounds, which do not display these features. Cu^{0} and Cu^{+} exhibit a $3d^{10}$ electronic configuration, meaning their 3d orbitals are fully occupied. As a result, no additional electronic transitions can occur during photoionization, which accounts for the

absence of shake-up satellites[20]. As a result, the Cu 2p region is a valuable tool for identifying the presence of copper in its most oxidized form. The Cu $2p_{3/2}$ peak corresponding to Cu^{2+} is also shifted to a higher binding energy (933.6 eV [16], indicated by the dotted line)

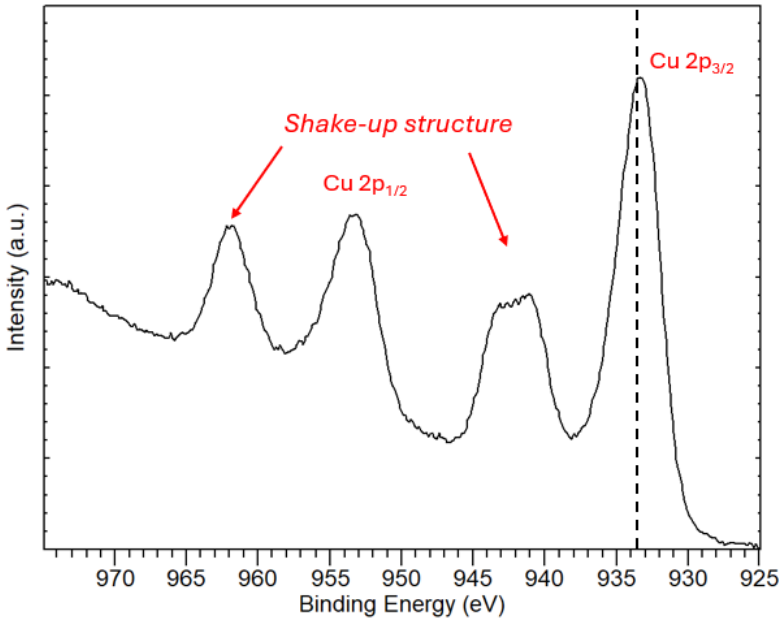

Figure 6 : Shake-up structure of the Cu 2p region from CuO

1.1.6. Surface sensitivity and IMFP

XPS is a surface-sensitive technique. Although the incident X-rays can penetrate relatively deep into the material, about few µm, only electrons generated near the surface escape without significant energy loss. The deeper the photoelectrons are emitted from within the sample, the more inelastic collisions they experience, which leads to a reduction in their kinetic energy [21] . In Figure 7, only the unscattered or elastically scattered electrons labelled "a" are responsible for the main O 1s peak. They do not undergo any collisions and thus retain their full kinetic energy. Slightly below the surface, the "b" electrons experience at least one inelastic interaction. As a result, they emerge with lower kinetic energy and thus appear at higher binding energies. They contribute to the vertical step in the blue hatched area of the spectrum, known as the background. The "c" electrons, located even deeper, are subjected to

numerous inelastic collisions and consequently fail to escape from the sample and so doesn't participate to the spectra.

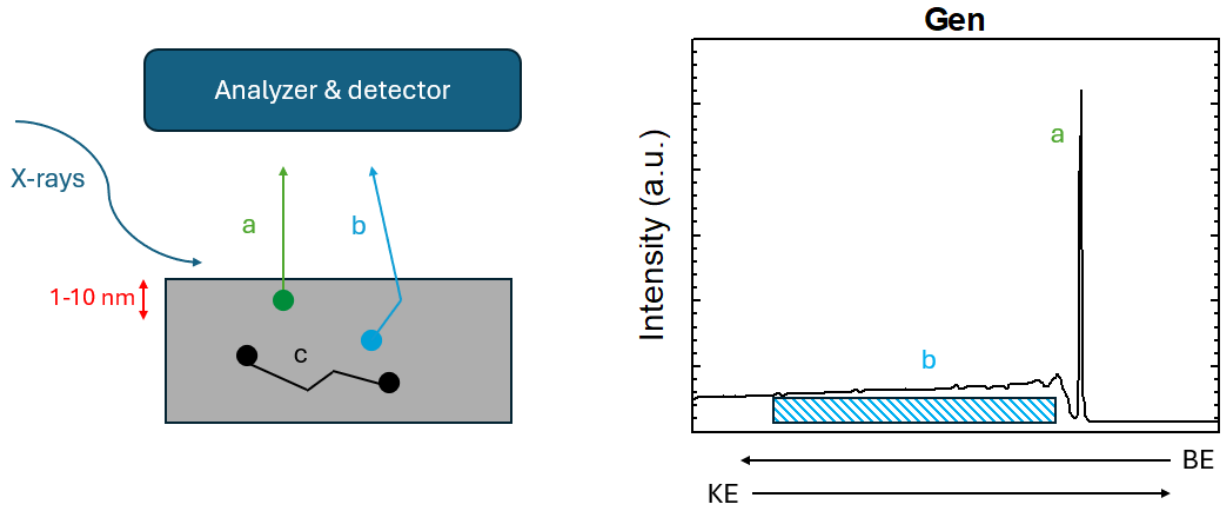

Figure 7 : Schematic view of the three possible fates for photoelectrons formed in a material, as a function the depth and corresponding typical XPS spectrum(a) without collision, produce XPS photoelectron peak. (b) at least one inelastic collision, contribute to the background. (c) undergo multiple collision, do not escape the sample

The surface sensitivity of XPS is determined by how deep an electron can be generated and still escape without inelastically scattering. The intensity of the electron signal emitted at a depth d can be written as [21,22]:

$$I_s = I_0\, e^{-\frac{d}{\lambda \cos\theta}} \tag{5}$$

With I_s, the detected intensity and λ is the inelastic mean free path (IMFP) in the sample, defined as *"average distance that an electron, with a given energy, travels between two successive inelastic collisions"* [22]. θ is the emission angle.

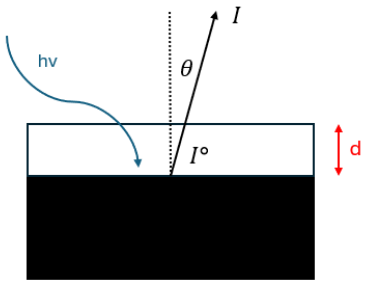

Figure 8 : Geometry of photoelectron emission in XPS, with incident photon energy hv, emission angle θ, and detected intensity I.

And the probability $\frac{I}{I_0}$ that an electron escapes the sample at depth d in a direction making the angle θ without energy loss is given by:

$$P(z) = e^{-\frac{d}{\lambda \cos\theta}} \quad (6)$$

Where $\frac{d}{cos\theta}$ is the distance travelled by the photoelectron in the solid. As θ is typically 0° for standard measurements, the probability of an electron escaping is usually approximated by:

$$P(z) = e^{-\frac{d}{\lambda}} \quad (7)$$

When $d = \lambda$, the probability is therefore 0.368. That means that 36.8 % of the photoelectrons will reach the surface from this depth without experiencing inelastic scattering.

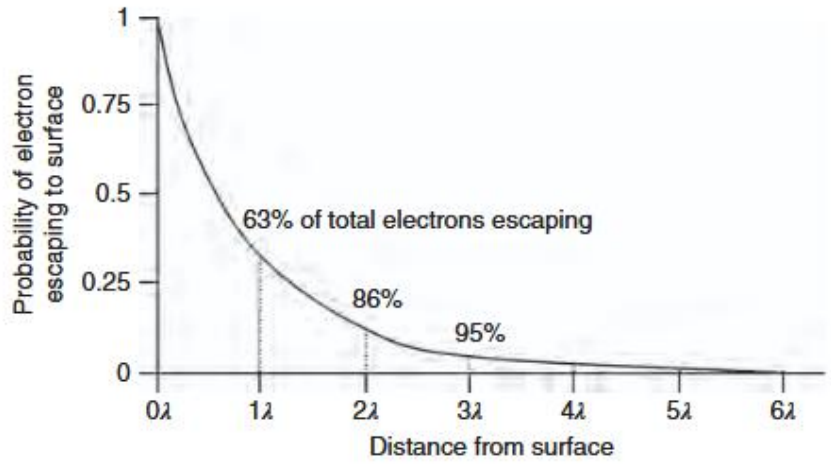

Figure 9 : Exponential relationship between the probability of exiting the sample without energy loss and the depth of emissions expressed in IMFP[10].

As shown in Figure 9, about 63% of photoelectrons come from a depth of one λ and over 95% from within three λ. For electron energies ranging from 100 to 1000 eV, λ in copper varies between 1 and 4 nm[23]. Consequently, 95% of the detected signal originates from a depth of approximately 3 to 12 nm. Although X-rays penetrate deeply, only electrons from near the surface escape and are detected, making XPS a highly surface-sensitive technique.

1.1.7. Limitation of XPS

One of the main limitations of conventional XPS is the requirement to operate under ultra-high vacuum (UHV) conditions, typically around 10^{-9} mbar. The main reason is due to the very short electron mean free paths in gas. Indeed, photoelectrons have low kinetic energies and

are easily scattered or absorbed by gas molecules. In a gaseous environment, the IMFP of these electrons can be very low[24]. For example, the λ of electron of 1000 eV in 1 bar of N_2 is approximately 0.15 μm[25], making it impossible for them to reach the detector (about 1m) without significant energy loss. Working in UHV greatly increases the IMFP, often to several kilometres, allowing electrons emitted from the sample surface to travel unobstructed to the detector.

Moreover, UHV is also necessary to protect the sensitive components of the instrument, such as the X-ray source and electron detectors[6]. UHV is also use to avoid contamination of the sample surface. Although XPS can still analyze partially contaminated surfaces, since contamination itself can be characterized, some instruments are equipped with in-situ cleaning systems, such as ion sputtering, that allow the surface to be cleaned directly inside the vacuum chamber before measurement[9].

Consequently, the sample must be UHV-compatible and fully outgassed before analysis. But, in practice, most samples are prepared and introduced under ambient conditions, meaning they are almost always covered with a thin layer of adsorbed water or hydrocarbons from air exposure. This strict vacuum requirement comes with a major drawback: it prevents the study of samples under realistic, application-relevant conditions. It makes it impossible to perform analyses in the presence of reactive gases like O_2 or H_2. This is a significant limitation in the field of heterogeneous catalysis, where reactions typically occur at the gas–solid interface under ambient or elevated pressures.

1.2. Evolution towards Near Ambient Pressure XPS

Near-Ambient Pressure XPS has been around since the early days of electron spectroscopy, when experiments were carried out on gases at pressures of several millibars. However, despite its promise, the technique saw limited use for many years due to low data quality, and limited availability of appropriate instruments[26]. It remained possible mainly at synchrotron facilities, where the combination of high photon flux and advanced instrumentation allowed researchers to overcome some of these limitations[27,28].

More recently, NAP-XPS with lab source has re-emerged as a powerful technique to overcome the limitations of conventional XPS[29]. NAP-XPS allows measurements at pressures of up to several tens of millibars, significantly closer to ambient pressure. Facilitating in situ surface studies under more realistic environmental conditions. To put this into perspective, UHV-XPS operates around 10^{-9} mbar, while NAP-XPS can function about tens mbar, a difference of nine orders of magnitude. Bridging this gap represents a major engineering challenge, both in terms of instrumentation and maintaining electron energy resolution.

To address this, only the analysis chamber - where the sample is located - is brought to near-ambient pressure, while the rest of the system, including the X-ray source and the electron analyzer, is maintained under ultra-high vacuum. This compartmentalized design ensures that electron optics and analyzer performance are not compromised by gas-phase scattering or contamination[30] (See section 3.1.).

1.2.1. Electron IMFP in gas phase

The main challenge in NAP-XPS is that photoelectrons have very short inelastic mean free paths in gases, meaning they are rapidly scattered by gas molecules and lose part of their kinetic energy through inelastic collisions. These interactions can involve vibrational, rotational, or electronic excitations, or even ionization of gas molecules[31,32]. As a result, the intensity to noise ratio of the main peaks in the photoelectron spectrum decreases, and peaks may broaden on the low-energy side as observed on Figure 10.

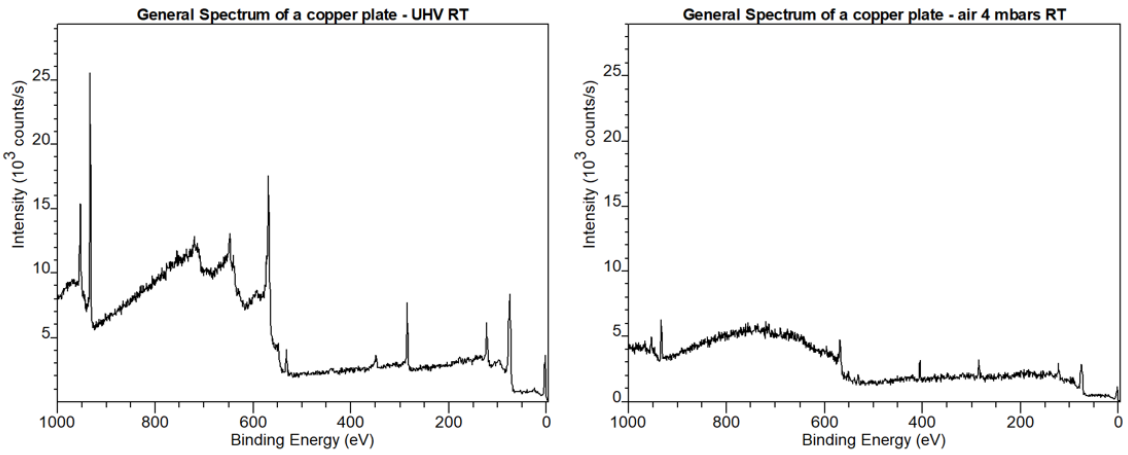

Figure 10 : comparison between general spectrum of a copper plate at a) UHV condition, and b) air 4 mbar condition

This strong signal reduction in gases is one of the main reasons why conventional electron spectroscopies have traditionally required UHV conditions. In NAP-XPS, the attenuation of photoelectrons by gas molecules in the chamber follows an exponential law, which describes a decrease in signal intensity with increasing pressure and path length[31,32]. The attenuation of photoelectron $\frac{I_p}{I_0}$ by the gas can be write as[24]:

$$\frac{I_p}{I_0}(E_k, P) = e^{-\frac{d}{\lambda(E_k,P)}} \tag{8}$$

Where:

- I_p is the photoelectron peak intensity at pressure P,
- I_0 is the intensity in vacuum,
- d is the distance travelled by the electron through the gas,
- $\lambda\,(E_k, P)$ is the electron IMFP in the gas dependent on pressure and kinetic energy,

Electron IMFP in gas phase λ_g is given by Equation 9[32], this shows the dependency at temperature T and pressure P. The total inelastic cross section σ ,which quantifies the probability of an inelastic collision between the incoming electron and gas molecules. It is usually expressed in square centimetres (cm²) and depends on the nature of the gas and the kinetic energy of the emitted electron[25,31]. K_b is the Boltzmann constant.

$$\lambda_g = \frac{K_b T}{\sigma(E_k) P} \quad (9)$$

1.2.2. Decrease attenuation from gas phase

To reduce the attenuation of photoelectrons by the gas phase and minimize inelastic scattering, one strategy has been to use higher-energy X-rays (hard X-rays, >2 keV) [29]. These photons generate photoelectrons with greater kinetic energy, which are less likely to undergo inelastic scattering and therefore have a longer mean free path. This increased IMFP allows electrons to travel through denser gas environments with less energy loss. Initially, such approaches were implemented at synchrotron facilities, using non-monochromatic sources, like Mo-Kα (17.479 keV) or Ag-Lα (2984.3 eV), to reach excitation energies above 10 keV. However, these sources are not easily accessible, as they require advanced infrastructure. Furthermore, as photon energy increases, the ionization cross-section drops sharply, significantly reducing the XPS signal. High-energy photons can also damage sensitive samples, limiting the practical application of this technique[27].

Typically, synchrotron light was used to perform ambient pressure photoelectron spectroscopy. But recently it is also possible to make NAP with classical lab source such as Al-Kα (1486,7 eV). Indeed, there are other ways to decrease gas phase attenuation[33].

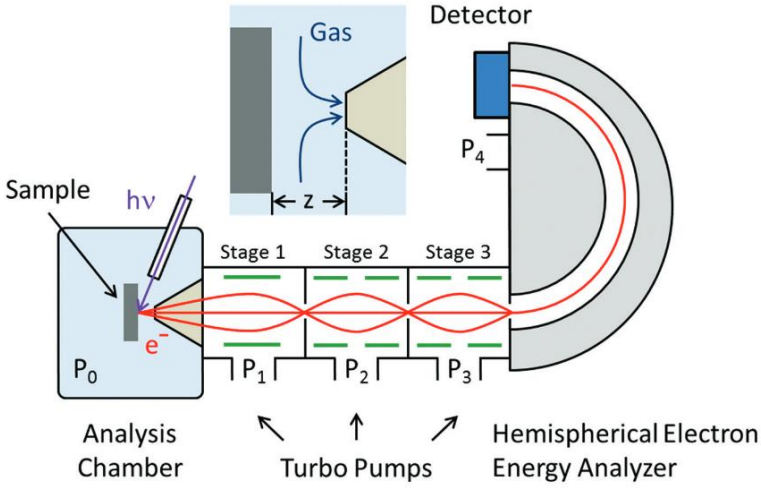

Figure 11 : Schematic of an NAP-XPS instrument [30]

One effective way to reduce gas-phase attenuation is by minimizing the distance electrons travel through the gas, z on Figure 11. This can be achieved by positioning the sample closer to the entrance aperture of the electron energy analyzer. By shortening the electron ‘s path, the signal intensity, represented by the ratio $\frac{I_p}{I_0}$ in Equation 8, is enhanced.

Additionally, to maintain UHV conditions around the electron energy analyzer, a differential pumping system is employed[26]. This system includes multiple pumping stages located between the analysis chamber and the detector, each providing a pressure drop of approximately three orders of magnitude, which is essential for preserving a strong signal. These stages are combined with electrostatic lenses that help to efficiently guide the electrons toward the detector[30]. Finally, the ionization efficiency is further optimized by tightly focusing the X-ray spot on the sample, ensuring it aligns precisely with the small aperture size[29].

This means that the gas between the sample and the analyzer’s entrance aperture is continuously evacuated by the first stage of differential pumping. Consequently, positioning the sample too close to the aperture lowers the local pressure, so the actual value just below the cone is often lower than the one set in the analysis chamber[34].

1.2.3. Energy loss peak

Although gas-phase attenuation is reduced, electrons still undergo scattering events as they travel through the gas. This scattering may give rise to additional, distinct features in the X-ray photoelectron spectra. These so-called energy loss peaks result from inelastic collisions, where photoelectrons lose specific amounts of kinetic energy by exciting electronic transitions in gas-phase molecules[32]. As a results additional structure appears at lower kinetic energy (higher binding energy) on the spectrum. The extent and nature of these features depend on the type of gas present and its pressure, as both influence the probability and energy characteristics of inelastic collisions[35]. This effect is particularly relevant for the Cu 2p core level in air. These photoelectrons are more prone to inelastic scattering, which leads to prominent energy loss peaks in their spectra, as shown in Figure 12.

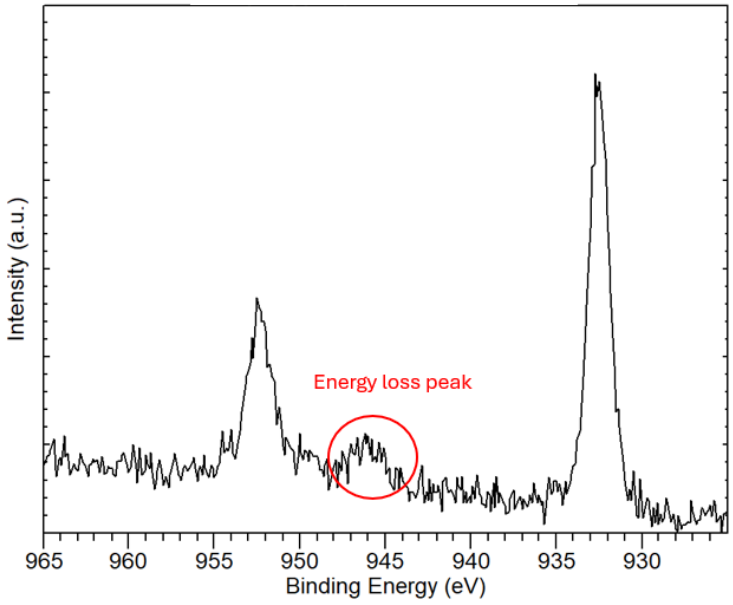

Figure 12 : Energy loss peak of the Cu $2p_{3/2}$ spectra in 2 mbar of air

1.3. Cu/SiO_2 Catalyst

As one of the first case of study for the newly NAP-XPS at UCLouvain, it was decided to focus on recently developed copper-based catalyst. The latter were designed in the context of bioethanol upgrading into acetaldehyde, via non-oxidative dehydrogenation[3].

The catalyst was synthesized using aerosol-assisted sol–gel (AASG) method[36], which enables excellent control over copper dispersion and particle size. This preparation route allows copper species to be embedded homogeneously within silica microspheres, leading to strong interaction between the metal and the support, and limiting sintering during calcinated and catalytic operation[37]. In the dehydrogenation reaction, ethanol is converted into acetaldehyde and hydrogen in the absence of oxygen. This transformation is of particular interest because it allows the production of acetaldehyde, a valuable chemical intermediate widely used in the industry, from renewable bioethanol sources[38].

After synthesis, the catalyst undergoes a two-step calcination to stabilize its structure and convert copper precursors into the oxide form. First, the dried powders are calcined in static air at 623 K for 3 hours, followed by a second calcination at 823 K for another 3 hours, both with a slow heating rate of 1 K/min. This careful thermal treatment serves multiple

purposes: it removes residual organic species, promotes the formation of CuO nanoparticles, and ensures the development of a stable and porous silica matrix. Ex situ analyses (XRD, XPS, chemisorption) coincided to suggest that Cu species, initially embedded into the silica matrix, migrate to the surface of the material during calcination. The gradual heating avoids sudden thermal shocks, which helps maintain small copper particle sizes and supports a homogeneous dispersion onto the silica network. The resulting catalyst featured high surface area and good thermal stability[3].

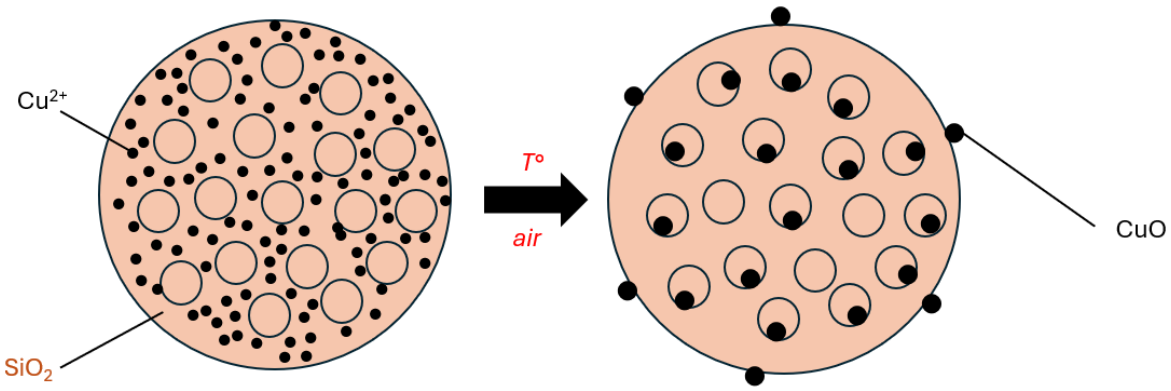

Figure 13 : Cu^{2+} ions are initially well dispersed within the silica matrix, but after calcination, they partially migrate and form CuO species at the surface of the catalyst. Schematic based on *Pamparao et al.*[3].

Before reaction, the Cu–SiO_2 catalysts were subjected to an in situ prereduction step to activate the copper species. This thermal treatment reduces CuO nanoparticles into metallic Cu° nanoparticles, wich are the actual active species for the dehydrogenation of ethanol [3]. This new catalyst demonstrated enhanced resistance to deactivation by sintering under reaction conditions. However, the various modifications in the catalysts at the different stages of preparation (pre-calcination, calcination, pre-reduction, reaction) are not fully elucidated at this stage. Understanding these, could lead to further improvement in catalyst development for this important reaction.

1.4. NAP-XPS in heterogeneous catalysis

As previously highlighted, gaining insight into the surface of a catalyst during a reaction is crucial for understanding the reaction mechanism. Therefore, a technique that offers high surface sensitivity and can analyze catalyst particles under gas-phase conditions is essential for revealing their surface chemistry during catalysis. Thus, NAP-XPS is extremely useful in the field of heterogeneous catalysis, as it enables real-time investigation under realistic reaction environments. For this reason, it has recently become increasingly used in catalysis research laboratories around the world[39]. Unlike conventional XPS, which is limited to UHV, NAP-XPS functions at pressures of several millibars, enabling the introduction of reactive gases such as O_2, CO_2, H_2, and H_2O during the analysis. This has led to major progress in the investigation of several key reactions, such as the Reverse Water Gas Shift [40] (RWGS), CO_2 hydrogenation [41,42] or alcohols oxidation [43] . Moreover, NAP-XPS allows researchers to monitor the formation and evolution of reaction intermediates (e.g., formate, carbonate, CO_2^- species in RWGS [40]) and track the chemical state of the active surface during the reaction.

1.5. Challenges and limitations in NAP-XPS

NAP-XPS faces several key challenges that must be carefully considered during experimental design and data interpretation. As previously mentioned, the main technical limitations is the transmission of photoelectrons in a gas environment. As pressure increases above a few millibars, the mean free path of electrons drastically decreases, leading to significant scattering and signal loss making quantification in NAP-XPS quite challenging. As an example, 1000 eV electrons lose 78% of their intensity when passing through 10 mbar of N_2.

Another major challenge concerns the precise positioning of the sample. The signal intensity is highly sensitive to the distance between the sample and the analyzer aperture[44]. Even minimal misalignment can result in a huge drop in signal. This issue is further complicated during *in situ* experiments at elevated temperatures. Heating the sample can cause thermal expansion, vibrations, or slight movements of the sample holder, all of which may affect the alignment and lead to unstable or non-reproducible results. Moreover, working in a gas-phase environment introduces additional complications. Surface contamination is more frequent under near-ambient conditions, particularly due to AdC or gas-phase reaction by-products[45].

These species can accumulate on the surface and interfere with the spectral signal, making interpretation more difficult and less reliable.

2. Objectives and strategies

This master thesis pursues several objectives. The primary goal was to master and operate the brand-new NAP-XPS instrument, which is intended to be used in different contexts (various types of catalysts, electrodes, thin film, solid electrolytes, membranes, etc.) in the near future. The master thesis was designed as a first careful approach to this complex analysis equipment, using model samples and focusing on operating parameters

To achieve this, preliminary experiments were conducted using a first model sample, a pure copper plate. This initial step is designed to familiarize with the technical aspects of the system, validate the reliability of the measurements, and assess the influence of the gas phase under near-ambient pressure conditions. In addition, the copper plate served as a reference for the subsequent analysis of Cu-based catalysts.

The final objective was to study a first catalyst of interest: the Cu-SiO_2 dehydrogenation catalyst. In this case, we set ourselves the goal to observe and elucidate the transformations that occur during thermal treatments, in particular the formation of CuO nanoparticles, the putative migration of Cu towards the surface, and the reduction to Cu nanoparticles.

Given the novelty of the subject, the experimental strategy was not always firmly established from the outset. However, it followed a logical progression: we first conducted a thorough analysis of a copper plate under various gas-phase and temperature conditions. Once this model system was well understood and the experimental approach validated, the catalyst was introduced into the NAP-XPS chamber to enable dynamic monitoring of the migration of copper species.

3. Materials and methods

3.1. Instrumentation

In this section, an overview of the key components of the NAP-XPS setup is provided, focusing on the X-ray sources and the electron analyzer. Installed in summer 2024, the system is based on the ProvenX-NAP platform from SPECS group, designed for surface analysis under near-ambient pressure conditions (up to 30 mbar). It includes a hemispherical PHOIBOS 150 NAP analyzer and specialized monochromatic X-ray source optimized for operando studies. It also features an additional x, y, z sample manipulator. A three-stage differential pumping system ensures electron detection at high pressure while preserving ultra-high vacuum where needed.

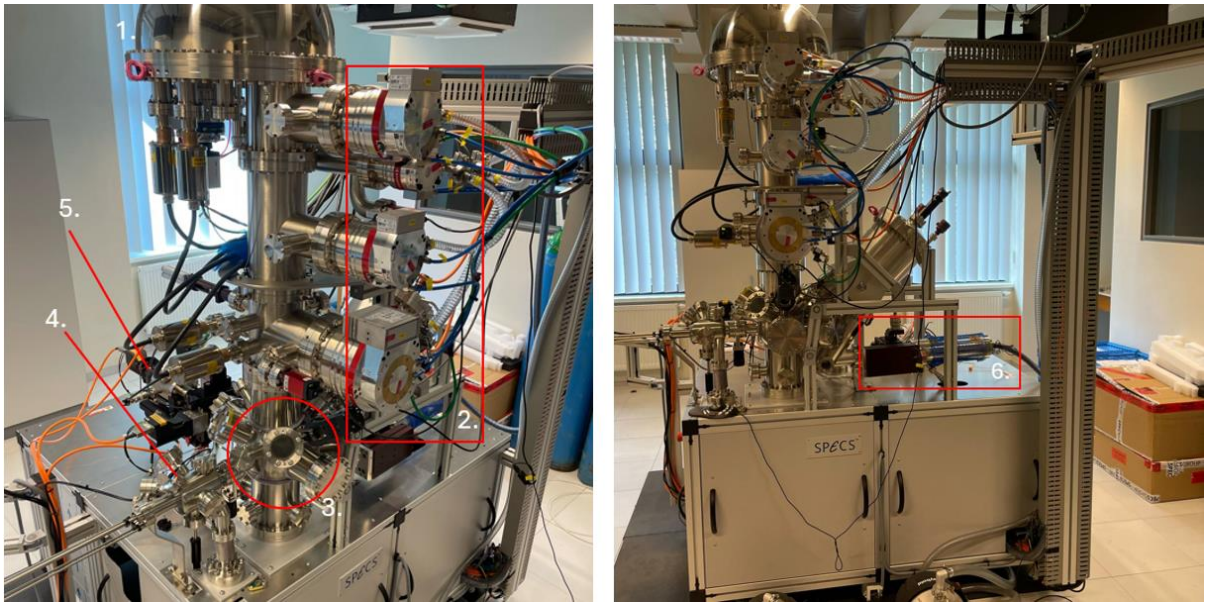

Figure 14 : Picture of the ProvenX-NAP: 1. Phoibos 150 NAP hemispherical electron energy analyzer, 2. Differential pumping system, 3. Analysis chamber, 4. Load lock chamber, 5. Sample manipulator, 6. XR50 NAP X-ray source

Reference measurements of the catalyst were carried out using a conventional UHV-XPS system: the SSX 100/206 Photoelectron Spectrometer (Surface Science Instruments), equipped with an Al Kα source. Although UHV analyses are also possible with the NAP-XPS system, the term 'SSI' is used throughout this work to clearly distinguish measurements performed with the conventional setup.

3.1.1. X-ray source

The ProvenX-NAP setup is equipped with the µ-FOCUS 600 NAP, a high-performance monochromatic Al Kα source operating at 1486.7 eV. This source uses a quartz single-crystal monochromator based on Bragg's law, with a 600 mm Rowland circle geometry, enabling precise energy selection and beam focusing. It delivers a high photon flux—up to 1.9×10^{10} photons/s—with an adjustable spot size between 200 µm and 1 mm.

The high-voltage anode responsible for X-ray generation operates in the keV range and must be effectively isolated from the elevated pressures present in the analysis chamber. To achieve this, modern lab-based NAP-XPS systems incorporate high-transparency X-ray windows that preserve ultra-high vacuum inside the source while allowing efficient photon transmission into the near-ambient environment. The X-ray window in the µ-FOCUS 600 NAP is made of silicon nitride (Si_3N_4) [29].

3.1.2. Gas pressure and sample distance

To mitigate the impact of high pressures on the IMFP of electrons, the sample-to-aperture distance should be minimized. However, to maintain stable pressure conditions, the sample must remain at least one aperture diameter away from the analyzer entrance (300 μm). This positioning ensures that the gas pressure directly above the sample remains 95% of the chamber pressure when operating in the viscous flow regime[46].

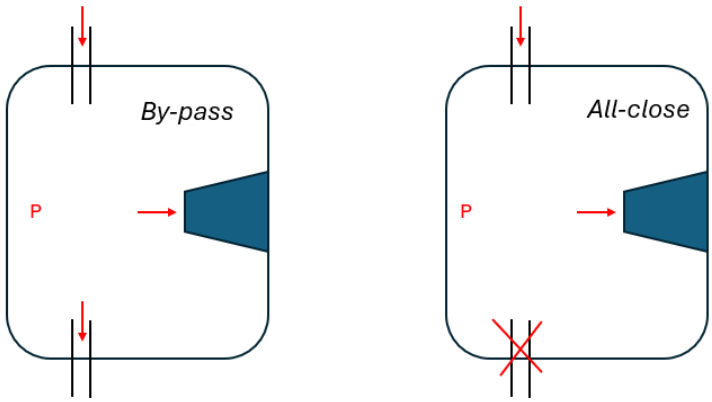

Figure 15 : Analysis chamber during NAP in a) By-pass and b) All-close

Two operating modes are available when switching to NAP conditions: the "bypass" mode, in which the gas is evacuated both through the cone and by one or more additional pump, and the "all-closed" mode, where the gas is pumped exclusively through the cone. We

chose to work almost exclusively in All-closed. Pressure control was quite challenging, especially since it was performed manually.

3.1.3. Electron energy analyzer

The system features the PHOIBOS 150 NAP hemispherical analyzer from SPECS, specifically designed for measurements under elevated pressure conditions. With a 150 mm mean radius and a true 180° geometry, the analyzer includes a differentially pumped electrostatic pre-lens and 3 pressure stages, allowing reliable electron detection at pressures up to 30 mbar while preserving ultra-high vacuum in the analyzer body. It supports a wide kinetic energy range (0–3.5 keV) with high energy resolution (<10 meV). The system can operate in both fixed and swept pass energy modes, with pass energies up to 550 eV [44], and the integrated 1D delay-line detector enables fast acquisition with high dynamic range.

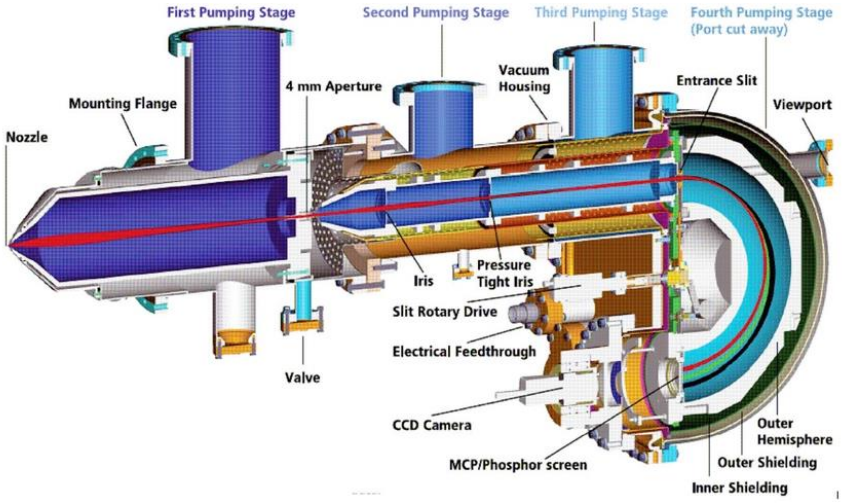

Figure 16 : Phoibos 150 electron energy analyzer with a differential pumping system from SPECS group

3.1.4. Sample preparation

Two types of samples were studied: a copper plate and catalytic powders, each requiring a specific preparation method.

Copper plate: The copper plate was mechanically polished to remove the native oxide layer, then rinsed thoroughly with isopropanol to eliminate any remaining surface contaminants before XPS analysis.

Catalytic powder: The catalytic powders were prepared by pressing them into small metallic cups using a manual press. The powder was first loaded into the cups and then compacted with the help of polyacrylate cylinders to ensure a uniform and stable pellet. We chose to work with a catalyst powder that had only undergone the first calcination step at 623K. At this stage, copper has not yet migrated to the surface, allowing us to carry out the second calcination directly within the instrument itself.

The samples are then mounted on a sample holder equipped with a ceramic heater and a thermocouple and then inserted in the load lock chamber. The sample can either be degassed in this chamber and transferred under vacuum into the analysis chamber—where the pressure is then increased to near-ambient conditions—or it can be introduced directly under gas flow, avoiding any exposure to vacuum.

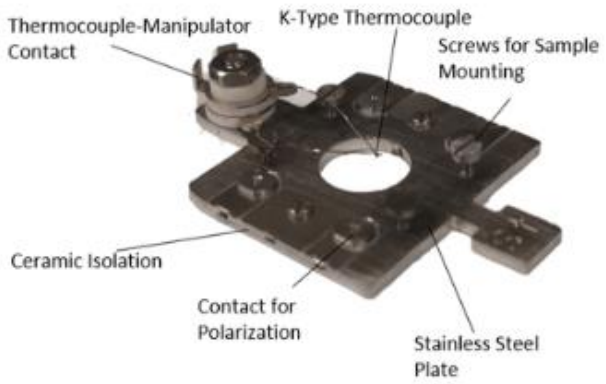

Figure 17 : Stainless steel sample holder

3.2. Data analysis

All XPS spectra were processed using the CasaXPS software. Background subtraction was performed using the Shirley algorithm. The C 1s spectrum for adventitious carbon (AdC) was decomposed into four components. Table 1 shows the constraints applied for the decomposition. GL(15) line shapes (a combination of Gaussian and Lorentzian functions with a 15% Lorentzian contribution) were used for all components. The Full Width at Half Max (FWHM) is it the distance between the two points on the curve where the intensity reaches half of the maximum value [47].

Table 1 : Parameters for decomposition of C 1s peak from adventitious carbon[18].

Component	C-C, C-H (A)	C-OH, C-O-C	C=O	O=C-O
Function	Aliphatic	Alcohol, ether	Ketones, aldehydes	Ester, acid
FWHM constr.	A	A x 1	A x 1	A x 1
Pos. constr (eV)	A	A + 1.5	A + 3	A + 4.2

Given the complexity of the O 1s spectrum, only two components were assigned: “O 1s Lattice” and “O 1s – Other”. Lattice oxide corresponds to oxygen atoms that are part of the crystalline structure of the metal oxide, typically forming metal–oxygen (M–O) bonds, for example in CuO or Cu_2O, located around 530 eV [48]. The “O 1s – Other” component includes contributions from oxygen species that are not part of the crystalline lattice. This may involve surface hydroxyl groups (OH^-), adsorbed water (H_2O), oxygen from AdC, or oxygen associated with surface defects or amorphous phases, located above 530 eV [49].

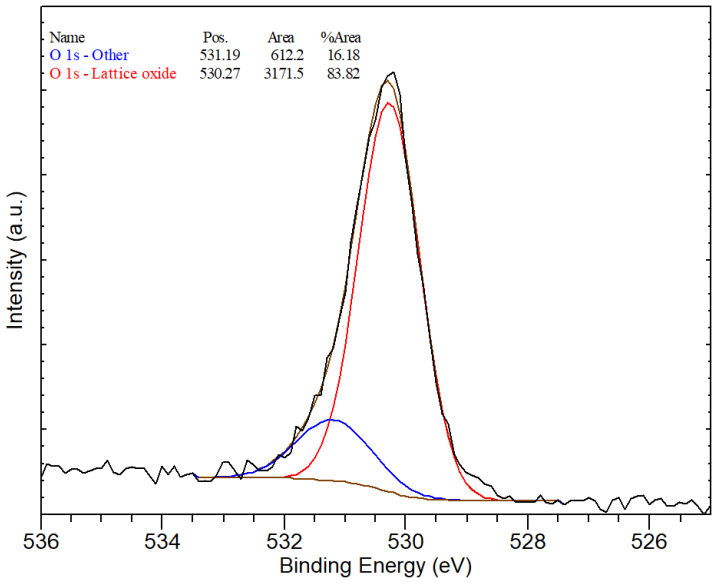

Figure 18 : O 1s region from CuO with 2 components: O 1s Lattice in red and O 1s Other in blue

The Cu 2p region was also processed using a simplified approach. Only the Cu $2p_{3/2}$ peak was deconvoluted. For the reduced forms of copper (Cu^+ and Cu^0), a simple background subtraction region was used. In the case of Cu^{2+}, the main peak was fitted with only one component, while the satellite feature was deconvoluted into two components.

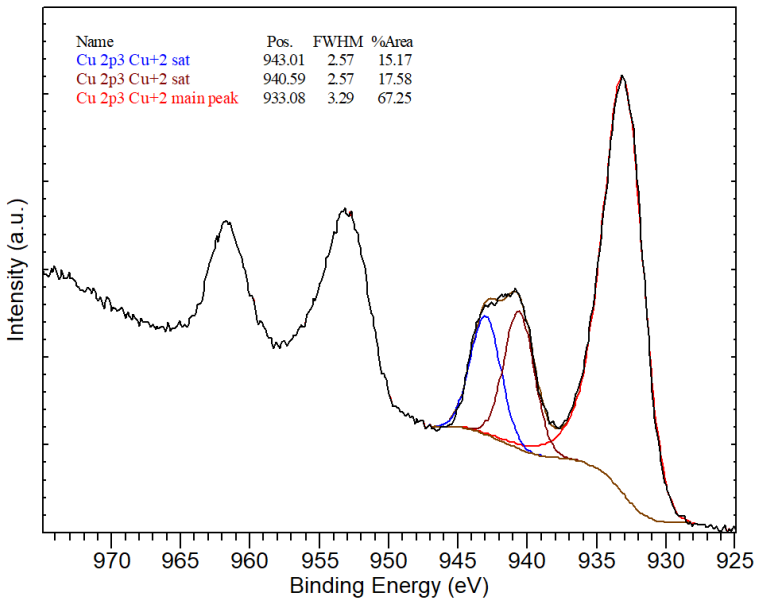

Figure 19 : Cu 2p region from CuO: 2 components for the satellite and one for the main peak

All other peaks, such as Si 2p, Cu 3p, and so on, were simply processed by applying a Shirley background without further peak fitting.

Elemental quantification was performed only for the samples analyzed under UHV using the following relative sensitivity factors (RSF) present in CasaXPS software:

Table 2: RSF for C 1s, O 1s, Cu $2p_{3/2}$ and Si 2p

Peak	C 1s	O 1s	Cu $2p_{3/2}$	Si 2p
R.S.F	1	2.93	16.73	0.817

3.3. Catalyst preparation

The Cu/SiO_2 catalysts were synthesized by Giovanni Pamparao following this protocol[3]. The preparation involved two separate precursor solutions. Solution A consisted of ethanol, distilled water, and a small amount of the nonionic surfactant Pluronic® F127. Solution B was prepared by mixing tetraethyl orthosilicate (TEOS) with an aqueous hydrochloric acid solution adjusted to pH 2 by dilution of concentrated HCl. Both solutions were stirred overnight before being combined and mixed thoroughly. Copper nitrate hydrate was then introduced in stoichiometric amounts to achieve the desired Cu loading.

The resulting sol was atomized using an aerosol generator operated at a constant air pressure of 207 kPa, producing fine droplets that were thermally dried in a quartz tube heated to 723 K. The solid product was collected on a membrane filter and subsequently calcined under static air in two steps: 3 h at 623 K followed by 3 h at 823 K, with a ramp rate of 1 K/min. The final catalysts were denoted A-CuXSi, where X corresponds to the nominal Cu loading (2, 5, 7.4, or 9.1 wt.% relative to the support mass).

4. Results and discussion

The results section is structured to follow the outlined strategy. First, the results related to the copper plate are presented and discussed. Then, those concerning the catalyst are addressed.

4.1. Copper plate analysis

4.1.1. First steps

Carbon contamination is a common phenomenon in XPS. AdC is found on almost all samples analyzed by XPS, particularly on transition metals such as copper [50]. Even after careful polishing, up to 70% of the total signal can originate from the C 1s peak as shown on Figure 20. This contamination mainly results from the adsorption of organic compounds present in the air. However, it also originates from the analysis chamber itself[51]. In UHV, the vacuum is never perfect and numerous residual molecules, mostly carbon-based, remain in the chamber and spontaneously adsorb onto the sample surface. This type of contamination is well known and is sometimes used to calibrate the spectra of insulating samples, generally without causing major issues. In our case, however, the thin carbon layer can act as a barrier that attenuates the signal of electron.

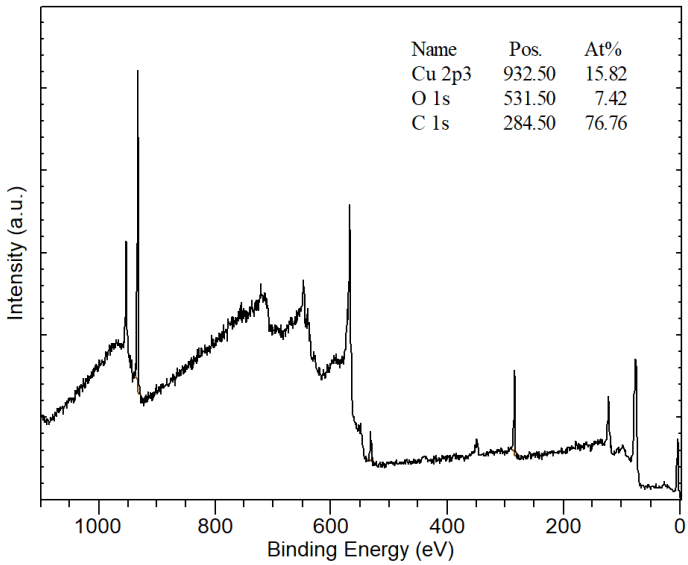

Figure 20 : Survey spectrum of a copper plate after sanding under UHV at room temperature

Our initial idea was therefore to use NAP-XPS to remove this AdC layer by heating the sample in a gaseous environment. To do this, the copper plate was placed in the analysis chamber at 1.8 mbar of air pressure, while being heated up to 515 K.

Figure 21a shows the survey spectrum of a copper plate exposed to 1.8 mbar of air at 298 K. The same three peaks as in Figure 20 are observed here: the Cu $2p_{3/2}$ peak at 932.5 eV, the O 1s peak at 530 eV, and the C 1s peak at 284.5 eV. A peak at around 405.5 eV is also observed in the N 1s region. This peak corresponds to the value reported in the literature[52] for gaseous N_2 from air, located at 406 eV. Figure 21b shows the three high-resolution windows corresponding to the three peaks of interest. The C 1s peak from adventitious carbon, exhibits four components typical of organic contamination carbon. The O 1s region displays a main peak around 530 eV and a smaller one near 539 eV, which corresponds to the O 1s binding energy of gaseous O_2 from air reported in the literature [52]. The detected oxygen may arise from various sources: the oxide layer on the copper surface (Cu_2O), copper hydroxide (CuOH), or oxygen associated with oxidized carbon contamination. Since the deconvolution of the O 1s peak is relatively complex, we opted for a simplified model using only two components: lattice oxygen bound to copper, and a second contribution, labelled “other”, encompassing both hydroxides and oxygen species related to carbon contamination. Despite polishing the copper plate, a strong metallic component is still observed in the O 1s region. This can be explained by the fact that when a copper surface is exposed to air, even for a short time, a very thin native oxide layer forms spontaneously[53]. The Cu $2p_{3/2}$ peak appears at 932.5 eV, which corresponds to copper in its reduced form Cu^0 and Cu^+. A structure also appears beyond 945 eV, which corresponds to the energy loss peak of Cu $2p_{3/2}$ electrons in air. It should not be mistaken for the satellite peak typically observed in the presence of Cu^{2+}.

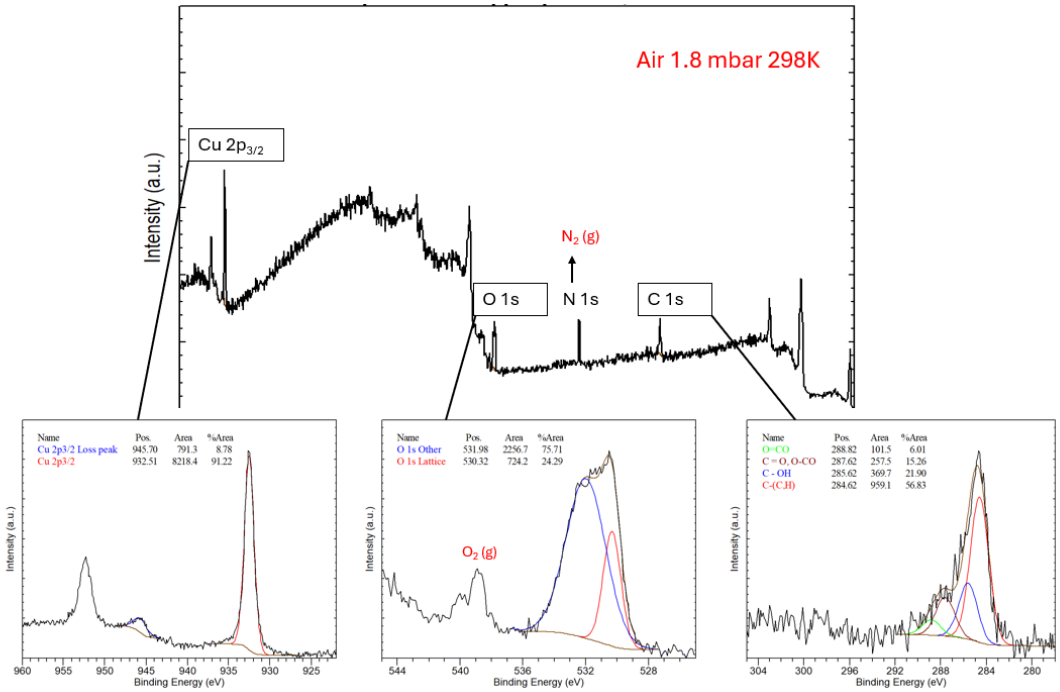

Figure 21 : a) Survey spectrum of a copper plate under 1.8 mbar of Air at room temperature. b) High-resolution spectra of, from left to right, Cu 2p, O 1s, and C 1s regions under 1.8 mbar of Air at room temperature.

Adventitious carbon contamination can be relatively easily removed by heating in air. Up to 373 K, the carbon content remains stable. However, starting at 373 K, a gradual decrease in the carbon signal is observed on Figure 22, and by 515 K, the carbon appears to be eliminated, suggesting full desorption or oxidation of the adventitious layer. One might assume that heating carbon in air leads to complete oxidation. However, such a reaction would produce a peak around 293.7 eV according to literature [54] in the C 1s spectrum, corresponding to CO_2. Since this peak is not observed — unless it is hidden in the noise — it is more likely that the process involves simple thermal desorption.

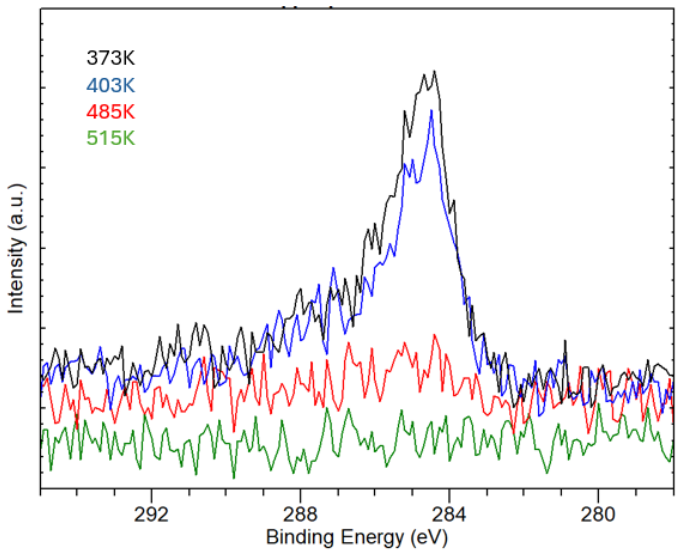

Figure 22 : C 1s spectrum at 373K, 403K, 485K and 515K.

Figure 23a shows the normalized O 1s spectra recorded on the copper plate at different temperatures. A gradual shift of the peaks toward the reference value of 530.2 eV (indicated by the dotted line) can be observed, which corresponds to the characteristic O 1s signal of Cu_2O [48]. Additionally, the FWHM decreases, reaching 1.25 eV at 515 K, indicating an increasing contribution of the metallic component in the oxygen signal. Indeed, values around 1.2 eV are also reported in the literature[48].

Although this lower FWHM could be attributed to the oxidation of the copper plate, the Cu 2p region at 515 K still indicates a predominantly reduced state. In reality, it is primarily due to the progressive removal of the organic contaminant (labeled 'Other' in the spectra). As a result, the 'Lattice' component becomes more prominent. As shown in Figure 23b, at 515 K, the metallic component accounts for over 80% of the oxygen signal, compared to only 25% before carbon desorption, as shown in Figure 21b. However, this increase is not solely due to the desorption of AdC, but also to the onset of oxidation of metallic copper into cuprous oxide (Cu_2O).

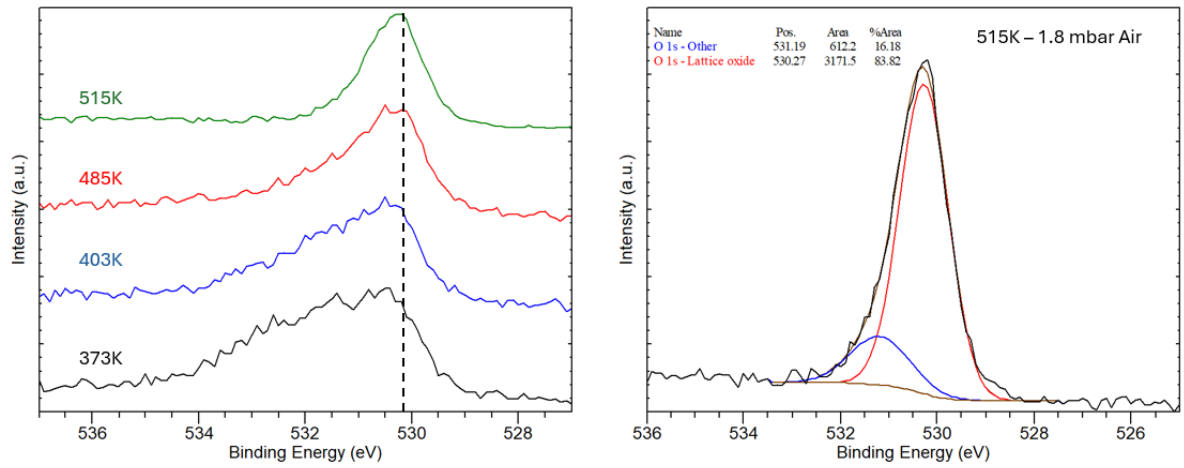

Figure 23 : a) O 1s spectrum at 373, 403, 485 and 515K. b) O 1s deconvoluted spectra at 515K

As shown in Figure 24, the intensity of the Cu $2p_{3/2}$ signal more than doubles at 515 K following the removal of the contamination layer. This carbon layer increases the path length electrons must travel and causes inelastic scattering that prevents some of them from reaching the detector. Since XPS probes only the top (~ 10 nm) of a material, part of the signal is lost when electrons cannot escape through the surface layer.

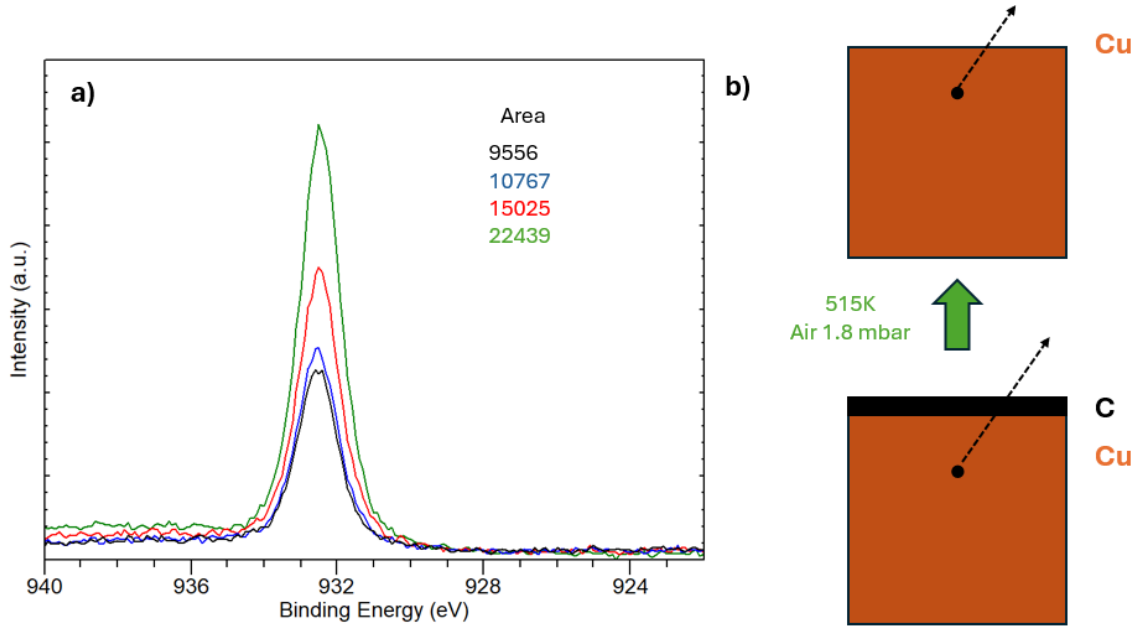

Figure 24 : a) Cu 2p3/2 at 373, 403, 485 and 515K. b) Schematic representation of AdC on copper plate surface acting as an electron barrier, which is removed upon heating to 515K

Moreover, as soon as heating is stopped and UHV conditions are re-established, carbon contamination quickly reappears on the surface, as shown in Figure 25. After the heating is stopped, the copper surface begins to cool down. At lower temperatures, the surface becomes more favourable for adsorption[55]. Although the contaminant carbon was desorbed during heating, it remains present in the analysis chamber. As a result, some of these residual carbon species can re-adsorb onto the now-cooled surface, leading to a rapid reappearance of the carbon signal in the C 1s region.

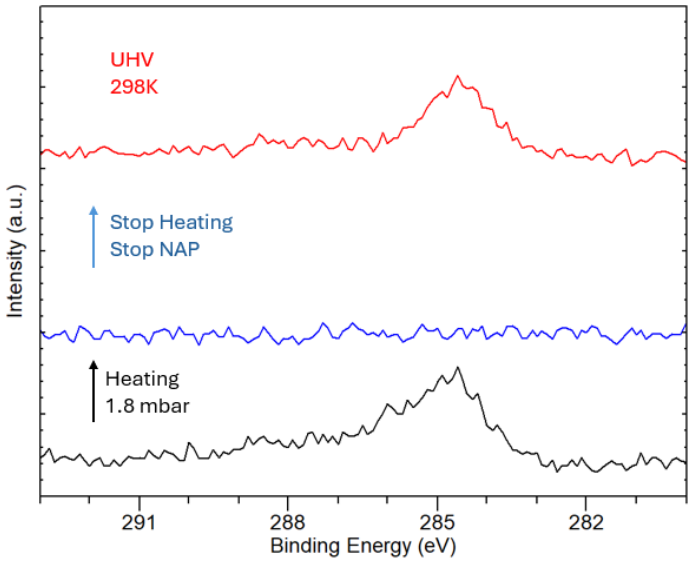

Figure 25 : C 1s spectrum before heating in black, in blue after heating, and after restoring UHV conditions and cooling

Removing the contamination layer is especially important in NAP-XPS, where some electron signal is already attenuated by scattering in the gas phase. Any additional signal loss due to surface contamination is therefore not acceptable. Fortunately, AdC desorbs easily upon heating under any gas tested. Carbon desorption was highly sensitive to the experimental conditions. The temperature needed to fully remove carbon depended on the gas type, pressure, and heating duration.

4.1.2. Thermal oxidation of copper

After cooling down the plate and restoring UHV conditions, a new heating cycle was performed under air. Although the target pressure was 2 mbar, it fluctuated and reached up to 2.37 mbar. Carbon desorption started at 373 K. As the copper plate continues to be heated under air, the chemical composition of the surface changes. Indeed, Figure 26 shows the evolution of the Cu 2p region during the gradual heating of the copper plate under 2 mbar of Air. A characteristic satellite peak of Cu^{2+} appears around 500 K. As the temperature increases further, this satellite peak becomes more pronounced. In addition, the main peak shifts towards the reference binding energy reported for CuO, 933.3-933.6 eV [16].

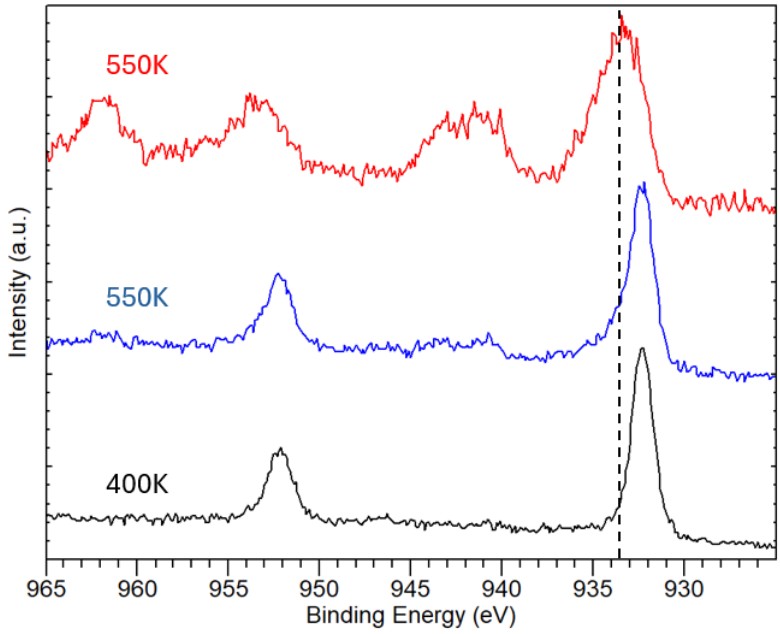

Figure 26 : $2p_{3/2}$ spectra recorded during progressive heating under 2.37 mbar of air. The characteristic satellite feature of Cu^{2+} becomes visible around 500 K.

Similar results were obtained by heating the plate under 2 mbar of O_2. Figure 27 presents the high-resolution spectra of the Cu $2p_{3/2}$ and O 1s core levels after oxidation in 2 mbar of O_2 up to 600 K. Starting at 500 K, the characteristic satellite features of Cu^{2+} become clearly visible in the Cu $2p_{3/2}$ region, accompanied by a shift of the main peak toward 933.4 eV. The spectral shape and peak positions are highly consistent with those of CuO, which typically displays a strong satellite structure and a main peak around 933.3–933.6 eV. This interpretation is further supported by the O 1s spectrum, where the main component at 529.3 eV matches reported binding energies for CuO. The peak at 539 eV corresponds to gaseous O_2.

Altogether, these spectra clearly confirm the formation of CuO during thermal oxidation in an oxygen atmosphere.

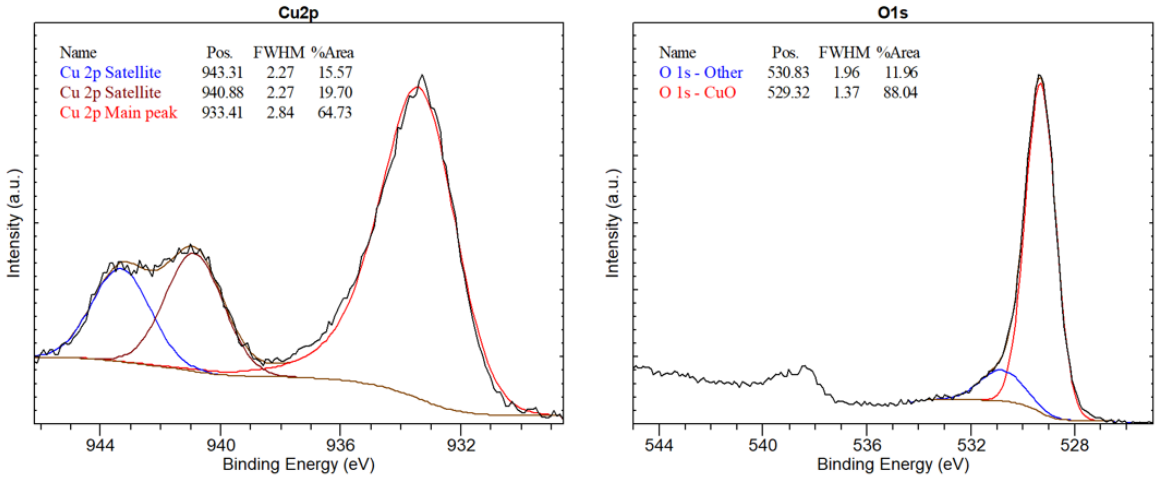

Figure 27 : Left, Cu $2p_{3/2}$ region with the characteristic satellite peak of Cu^{2+} after oxidation at 600K under 2 mbar O_2. Right, O 1s region after oxidation at 600K under 2 mbar O_2 with the main peak and the gaseous oxygen at 539 eV.

Interestingly, similar oxidation results were obtained under 2 mbar of air and 2 mbar of pure O_2, despite the lower oxygen partial pressure in air. This supports the idea that, in this pressure regime, the amount of available oxygen does not directly control the reaction rate. These observations suggest that, within the investigated temperature range, the oxidation kinetics are not limited by the gas-phase oxygen pressure. Instead, the rate-limiting step is likely the solid-state diffusion of ionic species—such as Cu^{+}, Cu^{2+}, or O^{2-}—through the pre-existing oxide layer[53,56]. This diffusion process requires thermal activation, indicating that the overall oxidation mechanism is primarily governed by temperature-dependent transport phenomena within the solid, rather than by oxygen availability at the surface.

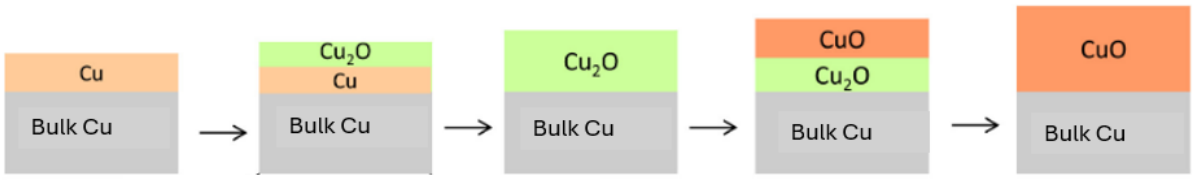

Figure 28 : Mechanism for forming a thin layer of CuO[56]

4.1.3. Signal attenuation

Strong signal attenuation was expected based on Equation 8 and 9. However, in practice, attenuation caused by the gas phase is inherently difficult to quantify, as it depends on multiple factors. This section aims to provide a quantitative assessment of this attenuation.

$$\frac{I_p}{I_0}(E_k, P) = e^{-\frac{d}{\lambda(E_k,P)}} \tag{8}$$

$$\lambda g = \frac{kT}{\sigma(E_k)P} \tag{9}$$

Figure 29 presents the signal loss observed for three core levels C 1s, O 1s, and Cu 2p when measurements are performed in different gas environments: Ar/H_2 (5%), O_2, Ar, and air. The signal loss is expressed as a percentage relative to the intensity measured under UHV, I_0 conditions and reflects the quantity of electron loss in gas phase.

$$Signal\ loss\ (\%) = (1 - \frac{I_p}{I_0}) * 100 \tag{10}$$

Where I_p is the intensity measured from the electron at 2 mbar of gas and I_0 the intensity measured under UHV. These intensities are measured as the area under the peak. All gas-phase measurements were conducted at a pressure of around 2 mbar at room temperature. It should be noted that electron attenuation in the gas phase is a highly complex phenomenon, and this data are insufficient to fully characterize it. Moreover, the actual pressure beneath the cone may differ from the nominal pressure, potentially affecting the accuracy of the results. This graph nonetheless offers a simplified estimation of the signal loss occurring in the gas phase.

The most striking observation is that, for all gases and for all electrons, there is a signal loss of more than 50%. This indicates that, at 2 mbar, at least half of the emitted electrons are lost through scattering in the gas phase. The most affected electrons are those from the Cu $2p_{3/2}$ level, with an average signal loss exceeding 60%, and reaching up to 70% in air. Cu $2p_{3/2}$ electrons have relatively low kinetic energy, around 555 eV, compared to other electrons in the spectrum, making them more susceptible to scattering in the gas phase.

Those results are higher than expected based on theoretical predictions. For example, the total cross section for O_2 can be found in the literature [31]; for electrons with a kinetic energy of approximately 500 eV, a value of 3.58×10^{-16} cm² is reported. Based on this, the mean free path of Cu $2p_{3/2}$ electrons in 2 mbar (200 Pa) of O_2 at room temperature is estimated to be 578µm. Under these conditions, the attenuation factor $(\frac{I_g}{I_0})$ is approximately 59%, indicating a signal loss of about 41%. Indeed, Equation 8 represents a simplified model based on several idealized assumptions. It considers a uniform gas distribution, a constant pressure, and straight electron trajectories, while neglecting complex effects such as local pressure gradients, multiple scattering events, and deviations caused by the geometry of the spectrometer[57].

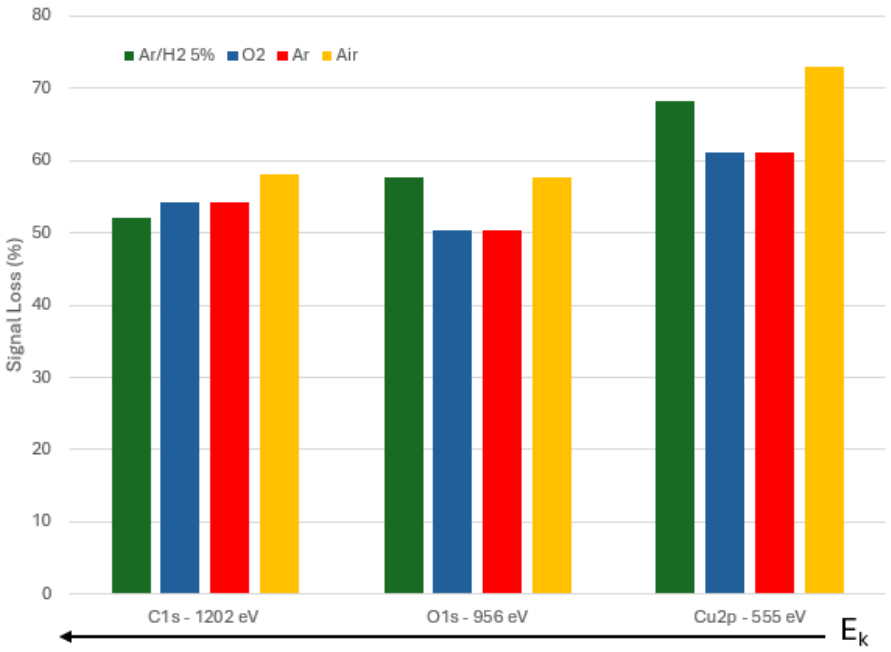

Figure 29 : Signal loss in percentage for 3 core levels electrons C 1s, O 1s and Cu $2p_{3/2}$ in different gas environment at 2 mbar.

In contrast, more energetic electrons, such as those from C 1s and O 1s, with kinetic energies of approximately 1200 eV and 956 eV respectively, are less affected by gas-phase scattering. It appears that C 1s and O 1s electrons experience quite similar attenuation, despite their difference in kinetic energy. This behaviour can be attributed to the complex, and often non-linear, relationship between electron kinetic energy and total scattering cross section [25,31]. As a result, an increase in kinetic energy above 1000eV does not systematically lead to a reduction in the total cross section and so reduction in the IMFP.

Among the gases tested, air results in the highest signal attenuation. However, it is important to note that this result cannot be generalized without caution. As already mentioned, attenuation from the gas phase is a complex phenomenon and its very dependant from the experimental condition in the analysis chamber which are sometimes difficult or impossible to control.

This attenuation of the photoelectrons complicates the quantitative elemental analysis of the surface and must be considered if a quantitative analysis is needed. Indeed, the electrons emitted by different elements have distinct kinetic energies, resulting in different IMFP and scattering probabilities when passing through the gas phase. Consequently, the attenuation is element-dependent, which distorts the measured atomic ratios compared to the true surface composition. To retrieve accurate quantitative data, it is therefore necessary to apply correction factors based on the attenuation factor (Equation 8), considering the gas composition, pressure, and temperature around the sample [58,59].

4.2. Catalyst analysis

In this section, the results obtained for the catalyst with NAP-XPS are presented. The initial objective—tracking the migration of copper species during calcination—could not be achieved. Despite this, the presentation of the data follows the chronological order in which the observations were made during the experiment.

Due to a malfunction of the thermocouple, temperature measurements were not available. Consequently, heating was conducted in current-controlled mode, and temperature values are reported in amperes. A current of 0.7 A was estimated to correspond to a temperature of approximately 500 K.

4.2.1. Cu 3p to follow the migration

In this study, numerous Cu 2p spectra were presented, as this peak is the most prominent and commonly used in XPS analysis of copper. However, the situation becomes more complex under near-ambient conditions. As previously mentioned, electrons emitted from copper's 2p levels have relatively low kinetic energy and these electrons are more susceptible to attenuation by gas-phase scattering. By applying. The photoionization cross section σ can be found in the literature[25]. For electrons such as Cu $2p_{3/2}$, with a kinetic energy of approximately 500 eV in N_2 (assuming air is composed solely of nitrogen), a cross section σ of 3.55×10^{-16} cm² is typically used. At a temperature of 298 K and a pressure of 10 mbar (1000 Pa). By applying Equation 8, the IMFP is approximately 116 μm. Using Equation 9, we can then calculate the quantity of electrons I/I_0 lost the gas phase. At this pressure, about 90% of Cu $2p_{3/2}$ electrons are lost due to scattering in the gas phase. Cu 3p electrons, on the other hand, have a significantly higher kinetic energy of approximately 1400 eV. This higher energy results in a longer IMFP, making them less susceptible to attenuation by the gas phase under near-ambient pressure conditions. For instance, in air at 10 mbar, the IMFP of Cu 3p electrons is estimated to be around 411 µm, corresponding to a signal attenuation of roughly 50%. This explains why Cu 3p can be sometimes preferred over Cu 2p in NAP-XPS studies, particularly when minimizing gas-phase effects is critical.

In addition, the Cu 3p peak appears around 77 eV in binding energy, which is relatively close to the Si 2p peak of the SiO_2 support at 103 eV. This proximity allows both signals to be captured within the same energy window as shown on Figure 30. If copper migrates to the

surface, the Cu 3p signal is expected to increase and to evaluate this, the Cu 3p / Si 2p intensity area ratio can be calculated. An increase in this ratio serves as an indicator of copper migrating to the surface.

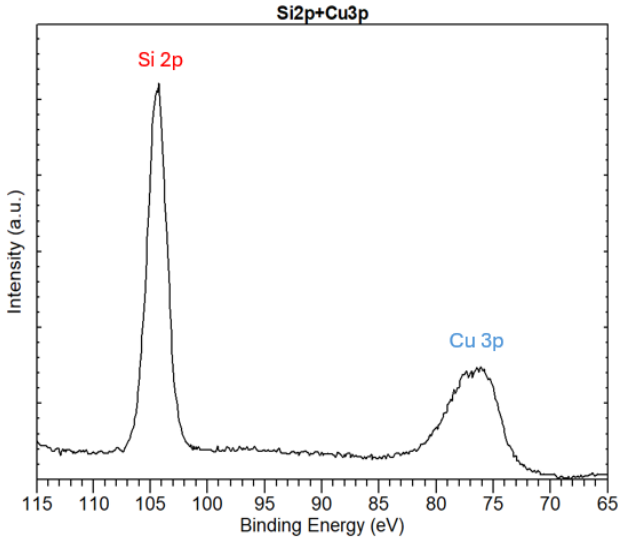

Figure 30 : Si 2p and Cu 3p on the same high-resolution window

4.2.2. Charge Neutralisation in NAP-XPS

Charge neutralization is an important parameter in XPS, but it has not been already discussed in this work because the copper plate is a conductive sample. However, Cu/SiO_2 catalytic powders are insulating samples. The emission of a photoelectron leaves behind a localized positive charge in the material. Since these materials lack sufficient mobile charge carriers, they cannot efficiently neutralize the charge buildup[9]. As a result, the surface becomes increasingly positive, leading to what is known as sample charging. As a result, Equation 1 becomes:

$$E_{\mathrm{k}} = h\nu - Eb - \phi_w - Ec \qquad (10)$$

For the copper plate, the charge correction term Ec is equal to zero, and the peaks are not shifted. However, Cu/SiO_2 catalytic powders are insulating samples, so the peaks are shifted due to the charge term. In NAP-XPS, charge neutralization is achieved through the gas phase. This process, known as environmental charge compensation (ECC), relies on the generation of ions, photoelectrons, Auger electrons, and secondary electrons from gas molecules induced by X-rays interacting with the gas[59,60]. These particles help to compensate

for the surface charging of insulating samples as shown in Figure 31. Charge compensation depends on a variety of factors, such as the nature of the gas, and its pressure.

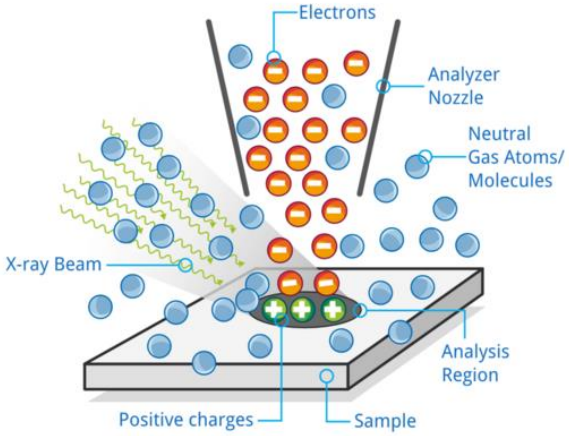

Figure 31 : Schematic representation of charge neutralisation by ECC in NAP-XPS[59]

The first step with the catalyst was therefore to test charge neutralization at different pressures. We worked exclusively under air or pure oxygen to further simulate a calcination process. The Si 2p spectra recorded at 7, 8, 9, 10, 11, and 12 mbar are shown in Figure 32. As the pressure increases, the peaks shift toward lower binding energies, approaching the reference (dotted line) Si 2p value for silica (SiO_2), which is 103 eV according to the literature[61]. This indicates that charge compensation improves with increasing pressure. This result is consistent, as a higher pressure means a greater amount of gas, and therefore more electrons that can be generated to compensate the surface charge. We also observe that the peak intensity decreases as the pressure increases. Indeed, higher pressure results in a higher density of gas layer that electrons must pass through, leading to more collisions with gas molecules and thus greater signal loss.

As shown in the position graph (Figure 32b), Above 10 mbar, the binding energy increases only slightly, by about 0.1 eV, eventually reaching 105.0 eV at 12 mbar, still 2 eV higher than the reference value of 103 eV for Si 2p in silica. This indicates that, even at this pressure, the number of electrons originating from the gas phase is still insufficient to fully neutralize the surface charge. Slight decrease in FWHM is also observed as the pressure increases. Effective charge compensation significantly improves spectral quality by minimizing surface charging effects. When applied, it leads to sharper spectral peaks and a reduced

FWHM. In contrast, insufficient charge compensation causes uneven energy losses of photoemitted electrons as they escape the sample, resulting in peak broadening and an increase in FWHM, thereby reducing spectral resolution.

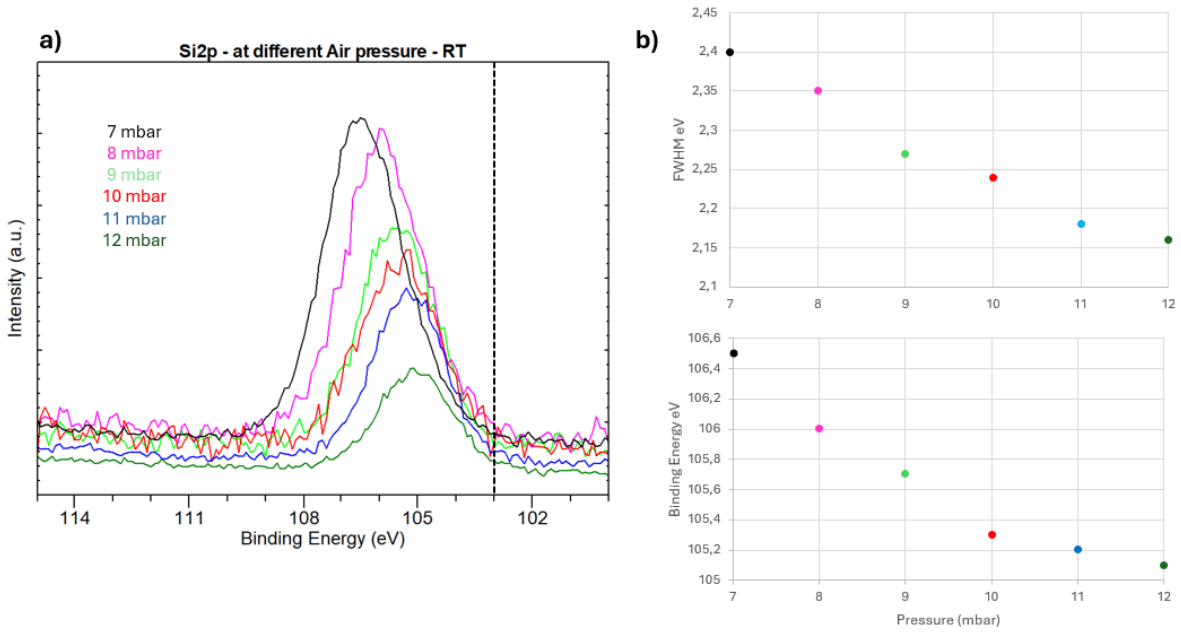

Figure 32 : a) Si 2p spectra measured in air at 7, 8, 9, 10, 11 and 12 mbar, the dotted line is the reference value for silica b) Plots of binding energy position (bottom) and FWHM (top) of Si 2p peak as a function of pressure.

This figure highlights the inherent complexity of charge neutralization in NAP-XPS, which is influenced by multiple interdependent factors. An optimal balance must be achieved between efficient charge compensation and the preservation of sufficient signal intensity. In this context of calcination, a pressure of 10 mbar appears to represent the most suitable compromise: it ensures effective charge neutralization—beyond which further improvements are minimal—while maintaining a relatively narrow FWHM and limiting signal attenuation.

4.2.3. Sample becomes conductor

When the sample was heated in 10 mbar air. It has been observed that between 0.5A and 0.7 A the Si 2p peak shifts significantly toward lower binding energies, reaching 102.9 eV, shown on Figure 33. These values are closer to those reported in the literature for Si 2p from amorphous SiO_2. Before 0.5 A, charge neutralization was solely achieved by electrons from the gas phase, resulting in a neutralisation about 105 eV in 10 mbar of Air. However, it appears that another mechanism is now contributing to charge compensation.

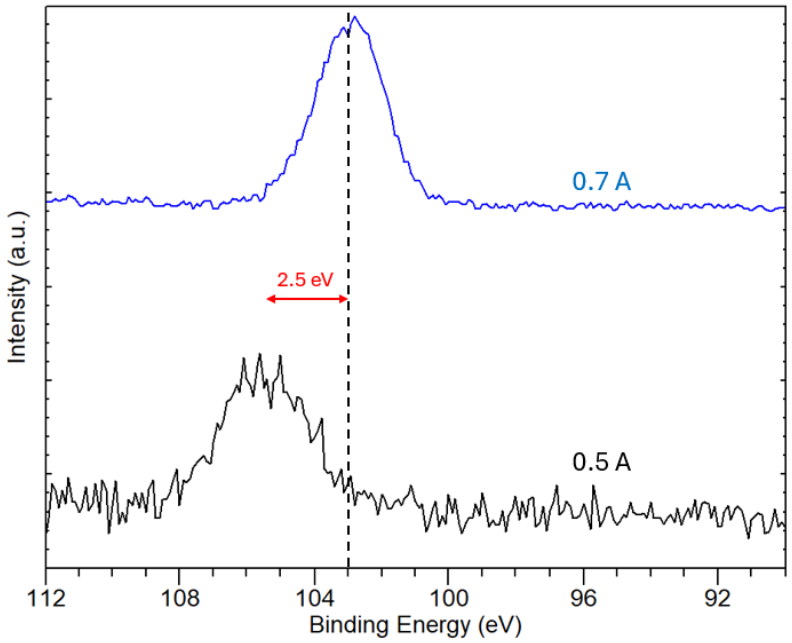

Figure 33 : Si 2p region at 0.5 A, in black and 0.7 A, in blue, under 10 mbar of Air

At room temperature, silica acts as an insulator, but when temperatures exceed 1300 K (1000°C), bulk silica can become conductive[62]. However, such high temperatures are never reached in the analysis chamber. A current of 0.7 A corresponds to value between 500 and 600K, which is insufficient to bulk SiO_2 to become conductive. In fact, at this temperature, only the extreme surface of the silica becomes conductive. Léo Philippe obtained similar results using a glass plate (amorphous SiO_2), which also becomes conductive when heated. This phenomenon therefore allows us to work at lower pressure and still achieving effective charge neutralization.

Similar results were obtained during heating under UHV conditions, as shown in Figure 34. When the sample is heated at 0.4 A, the spectral peaks return to their expected positions. Prior to this point, the survey spectrum is completely distorted. In the absence of gas charge compensation, the sample accumulate positive surface charges during photoemission. Since the charging is often spatially non-uniform, it leads to severe spectral distortion.

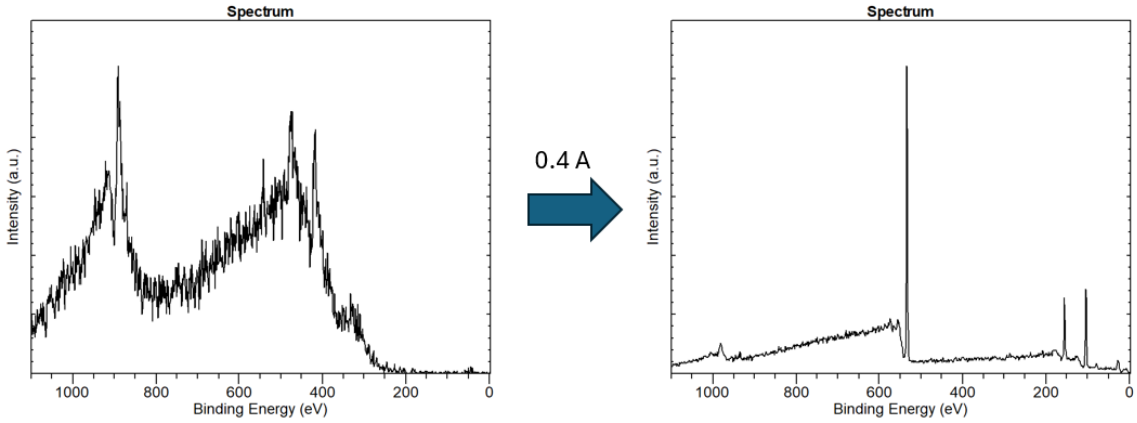

Figure 34 : Survey spectrum of Cu/SiO_2 catalyst before heating, and after heating at 0.4A.

The seemingly lower temperature required to compensate surface charging in UHV compared to NAP-XPS can be explained by the fact that, in the presence of a gas phase, part of the heat is dissipated through convective heat transfer. As a result, the actual temperature of the sample surface is lower than the temperature measured at the heating element.

4.2.4. Fluidic effect under the cone

During heating the sample under 10 mbar of air, when the current reached 0.7 A, the powder pellets, in the cups detached and stuck to the cone shown in Figure 35. This phenomenon can be explained by the expansion of the metallic sample holder due to the increase in temperature The diameter of the cup then becomes larger than that of the powder pellet, which was consequently drawn into the cone by the differential pumping system. To counter this phenomenon, we slightly modified the sample holder by adding a molybdenum plate on top of the cup to prevent the powder from being drawn into the cone. It was observed that heating the sample in the presence of the molybdenum plate led to a substantial improvement in signal intensity, in contrast to the sample heated without the plate.

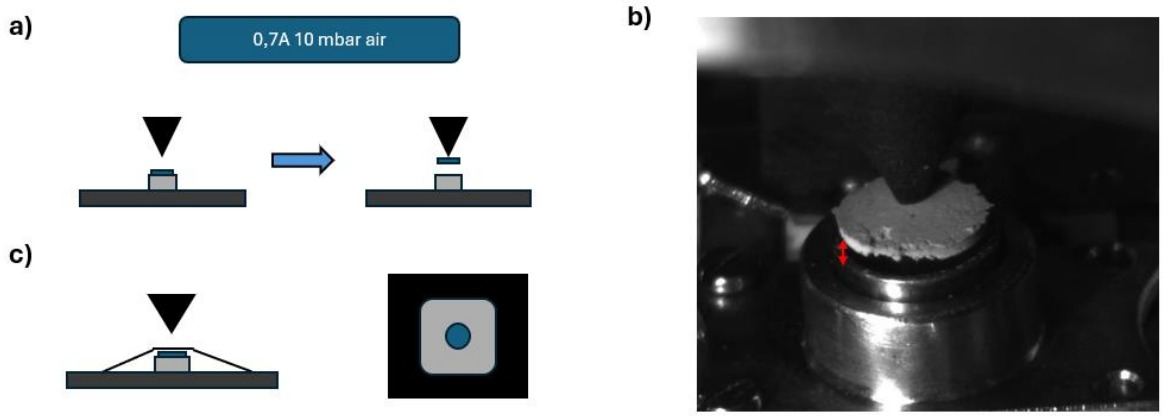

Figure 35 : a). When the sample was heated at 0.7 A, the pellets detached from the cups and were drawn into the cone. b) Picture showing the pellets sucked in by the cone into the cone. c) new sample configuration held in place by the molybdenum plate.

Figure 36 presents the Si 2p peak intensity when heating up to 0.7 A, a significant increase in signal intensity is observed when the sample was heated using the molybdenum plate. Although a slight improvement is also noticeable without the plate, its presence leads to a much more pronounced enhancement. Both measurements were carried out under identical pressure and heating conditions, using the same current-controlled mode.

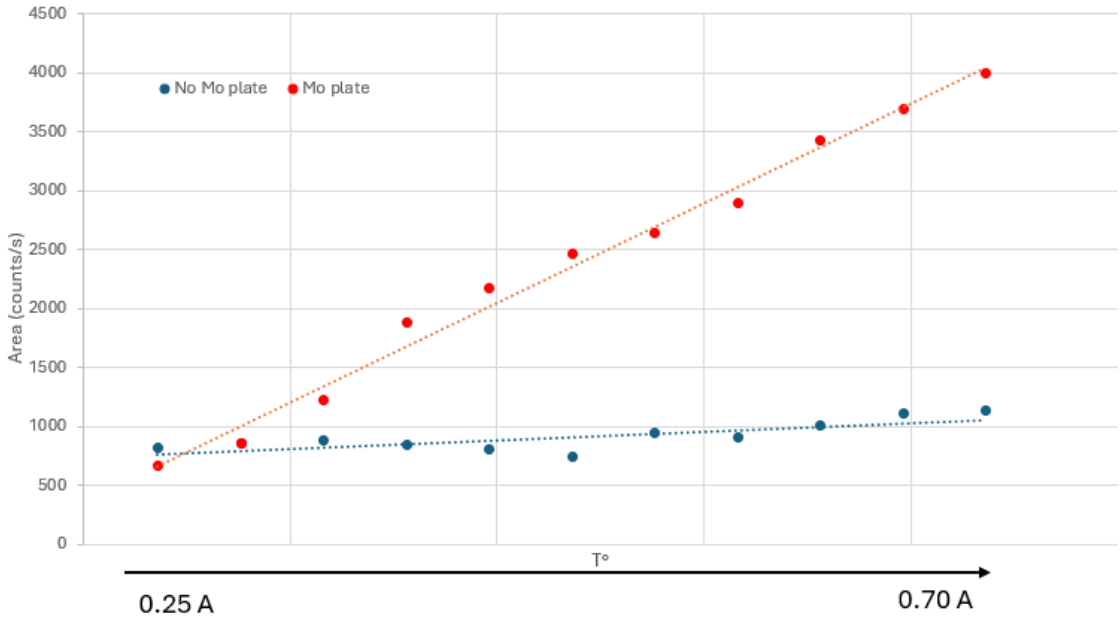

Figure 36 : Si 2p Intensity in area under the peak after background subtraction in counts/s when heated to 0.7A with the sample fixed by the Mo plate in red and the sample without the plate in blue.

Several factors may contribute to the observed increase in signal intensity with rising temperature. Indeed, the electron mean free path in the gas, given by Equation 9, which depends on both temperature T and pressure P.

As the temperature increases, the electron mean free path in the gas phase increases, leading—according to Equation 8—to an enhancement in the detected signal. Moreover, when a gas like air is heated, its density, $\frac{n}{V}$ on Equation 11, decreases. This reduces collisions with photoelectrons, and thereby further increasing the inelastic mean free path.

$$\frac{n}{V} = \frac{P}{RT} \tag{11}$$

These effects may account for the slight increase in signal observed for the sample without the molybdenum plate. However, these factors alone cannot account for the significantly greater signal enhancement observed in the presence of the molybdenum plate. A pressure drops induced by the plate perturbing the gas flux during heating could plausibly contribute to the observed increase in signal intensity. The pressure drops $P(T°)$ caused by the presence of the molybdenum plate when heating can therefore be modelled. By combining Equations 8 and 9, the following expression is obtained:

$$\frac{I}{I_0} = e^{-\frac{p\,d\,\sigma}{K_b T}} \tag{12}$$

The signal gain resulting from heating can be determined by calculating the ratio of the intensities measured before and after heating, as defined in Equation 13. Where I_1 and p_1 are the initial intensity and pressure before heating, T_1 is therefore room temperature. It is known that the actual pressure just beneath the cone is lower than the pressure measured analysis chamber. *Kahk et al.*[34] estimated that, at one aperture size, approximately 300 microns, the pressure drop is only 5%. So, this effect was neglected and p_1 is the analysis chamber pressure of 10 mbar. I_2 and p_2 are the intensity and pressure at T_2.

$$\frac{\frac{I_1}{I_0}}{\frac{I_2}{I_0}} = \frac{e^{-\frac{p_1 d\sigma}{K_b T_1}}}{e^{-\frac{p_2 d\sigma}{K_b T_2}}} \tag{13}$$

The distance d and the cross section σ, are assumed to be the same. I_0 , the intensity in UHV also. The intensity ratio then becomes Equation 14, and by rearranging we can obtain P_2 as a function of temperature T_2.

$$\ln\left(\frac{I_1}{I_2}\right) * \left(\frac{K_b}{d\,\sigma}\right) = \frac{P_2}{T_2} - \frac{P_1}{T_1} \tag{14}$$

$$P_2 = \left(\left(\ln\left(\frac{I_1}{I_2}\right) * \left(\frac{K_b}{d\,\sigma}\right)\right) + \frac{P_1}{T_1}\right) * T_2 \tag{15}$$

Equation 15 allows us to model the pressure drop induced by heating, which results from the disruption of gas flow by the molybdenum plate. For instance, at approximately 373 K, a pressure of 7.59 mbar is calculated—representing a loss of 25% compared to the initial value—which could account for this significant increase in signal intensity. While this model provides only a simplified estimation of the pressure drop caused by the plate, it clearly illustrates that the effective pressure between the sample and the cone aperture is significantly lower than the nominal 10 mbar in the chamber. However, it does not account for several important parameters, such as local turbulence, gas composition, or dynamic temperature gradients. Moreover, without an accurate measurement of the sample surface temperature, it remains difficult to reliably estimate the actual local pressure.

The presence of the molybdenum plate appears to significantly influence the actual pressure in the region beneath the cone. By more effectively heating the surrounding gas, the plate reduces air density and promotes the development of convective flows in the volume above the sample. As the gas becomes less dense, these convection currents can enhance the upward transport of gas toward the cone, which acts as the only outlet in the NAP-XPS "all closed" configuration. This accelerated movement may induce a localized pressure drop between the sample surface and the cone entrance. This drop in pressure would enhance the signal and this effect is expected to intensify with increasing temperature.

4.2.5. Migration of Cu species

Copper species migration could not be observed during calcination in air or under oxygen process in NAP-XPS. However, under vacuum conditions, such migration was clearly detected after successive heating. When the fresh catalyst was analyzed by UHV-XPS using the SSI equipped with a nickel grid, at room temperature, a Cu 3p / Si 2p intensity ratio of 0.14 was measured. The Cu 2p signal, originating from copper dispersed within the silica matrix, was observed in its oxidized form, as indicated by the presence of characteristic satellite structures (Figure 42).

When the sample was heated under vacuum, a noticeable increase in the Cu 3p signal intensity was observed. Figure 37a displays the Si 2p and Cu 3p spectral regions recorded during this thermovacuum process. Below 0.4 A, no meaningful signal could be detected, as the sample was not yet sufficiently heated to become conductive and remained prone to surface charging. The XPS spectra shown in the left panel were acquired in UHV at heating currents ranging from 0.5 A to 0.8 A. While the Si 2p signal remains relatively stable, the Cu 3p peak increases significantly with rising current, suggesting a progressive enrichment of copper at the surface. This interpretation is further supported by the Cu 3p / Si 2p intensity ratio plotted in the right panel, which rises steadily from approximately 0.55 at 0.5 A to nearly 0.85 at 0.8 A. These observations suggest that the signal enhancement is more likely attributed to the migration of copper species toward the surface, rather than to a general increase in photoemission intensity. This corresponds to a substantial rise from the initial Cu 3p/Si 2p ratio of 0.14 measured with SSI, in UHV at room temperature.

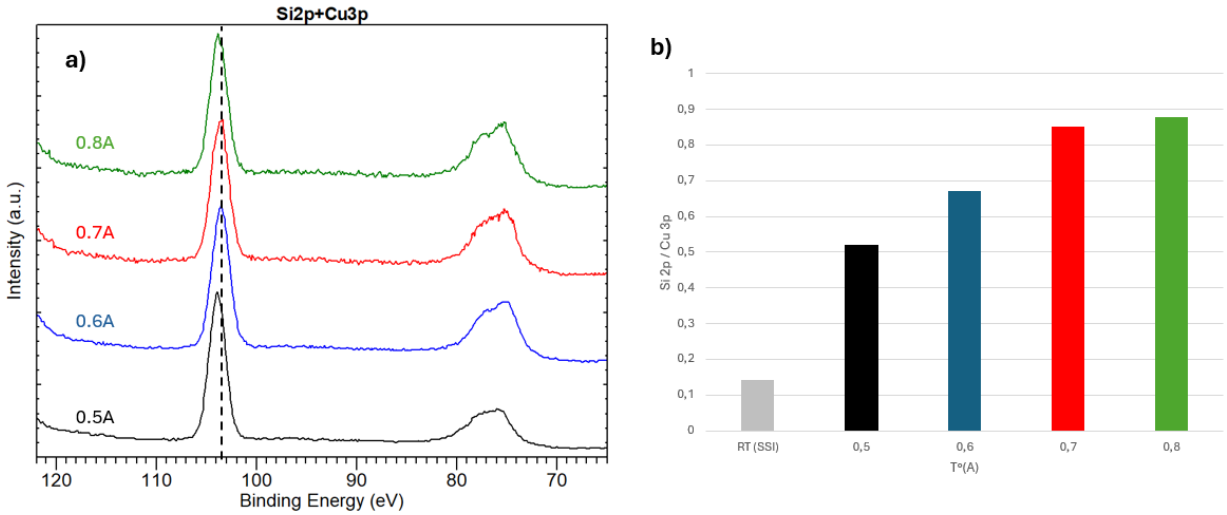

Figure 37: a) Si 2p + Cu 3p region at different current. b) Cu 3p/ Si 2p ratio at different current

The Cu 2p region reveals that copper is in a reduced state. While copper was initially introduced in the form of Cu^{2+} ions dispersed in the SiO_2 matrix, it undergoes reduction upon heating under vacuum conditions. This may be supported by the fact that *Amano et Al.*[63] reported that Cu^{2+} ions dispersed in supports such as Al_2O_3 can undergo self-reduction upon heating under vacuum, even in the absence of an external reducing agent. Copper migration to the catalyst surface during vacuum heating was observed only once, and it was never detected in NAP-XPS during calcination under air or pure O_2. Several explanations could account for this difference. Indeed, studies have shown that Cu^+ ions exhibit significantly higher mobility, compared to Cu^{2+} ions, in oxide support[64–66]. This is mainly due to the lower charge and weaker electrostatic interactions of Cu^+ with the silica network, which allow it to diffuse more easily. It is possible that, upon vacuum heating, dispersed Cu^{2+} ions within the matrix are reduced to Cu^+. This reduction may enhance their mobility within the silica framework, thereby facilitating their migration to the surface when heating in UHV. Further analysis by heating under a reducing atmosphere is required to confirm this.

When heating under O_2 or air, the temperature may not have been sufficiently high, or the duration not long enough, to enable the migration of Cu^{2+} species. In the case of the Cu/SiO_2 sample, a heating current of 0.9 A corresponds to an estimated temperature around 600-700 K. However, the heating current rarely reached 0.9 A, as the heating process failed often at 0.8 A. For comparison, the second calcination step in conventional treatments is

typically conducted at 823 K for 3 hours. Moreover, fluidic effects are known to occur between the sample and the cone. The gas flow in this region may contribute to heat dissipation, potentially lowering the actual temperature experienced by the sample.

4.3. General discussion

These results are often difficult to interpret and are not always reproducible, mainly due to the strong dependence on the experimental conditions in NAP-XPS. They are influenced by a multitude of interdependent factors, such as pressure, gas composition, temperature, and sample positioning. The presence of the gas phase significantly complicates the analysis. Furthermore, it is important to note that the actual pressure beneath the sampling cone differs from that in the rest of the chamber, which may affect the reliability of the data obtained. These findings clearly highlight the complexity introduced by adding gas under XPS conditions, making the measurements more challenging to control and interpret. As the instrument was newly installed, technical interventions were occasionally required — in particular, the heating system frequently malfunctioned — which reduced the effective measurement time and limited the amount of data collected

5. Conclusion and perspectives

This master's thesis served as a first case of study for the newly implemented NAP-XPS system for studies in heterogeneous catalysis. the technique remains highly sensitive to a wide range of interdependent experimental parameters. Our findings confirm that gas-phase scattering and local pressure gradients significantly compromise spectral quality and quantitative interpretation.

In a first step, a copper plate was used to become familiar with the instrument. It was observed that under gas flow, adventitious carbon desorbed upon heating, resulting in an overall increase in signal intensity. Thermal oxidation of the copper plate was also detected under 2 mbar of air and O_2. A simplified estimation of gas-phase attenuation was carried out. At 2 mbar, more than 50% signal loss was observed for the C 1s, O 1s, and Cu 2p electrons, with Cu 2p electrons showing the highest attenuation. In a second phase, a mesoporous Cu/SiO_2 catalyst was analyzed. The initial objective of observing copper species migration during calcination under O_2 or air could not be achieved; however, a single experiment was successfully performed under UHV conditions It was found that the sample becomes conductor when heating. A signal gain was also attributed to fluid dynamic effects occurring near the sample during measurement, we developed a simple model of the pressure drop. We found that the actual pressure between the sample and the cone aperture could be 20% lower than the analysis chamber.

As demonstrated by this work, the potential for improving NAP-XPS is considerable. However, if a few key areas were to be prioritized, efforts should first focus on achieving better control over experimental conditions to ensure data reproducibility. This includes a more precise investigation of the actual pressure between the sample and the analyzer cone. Additionally, it is essential to gain a deeper understanding of electron attenuation in the gas phase, by experimentally quantifying the number of electrons lost as a function of pressure and temperature, rather than relying solely on theoretical estimations.

Appendix

Loss of Signal in N2 for 1000 eV electrons

Table 3 : Signal Lost as a function of pressure in N2 for 1000 eV electrons from 300 microns

Mbar	P (Pa)	IMFP	micro	I/I°	Signal lost	%
1	100	0,001931	1930,704	0,856086619	0,143913	14,39134
2	200	0,000965	965,3521	0,732884299	0,267116	26,71157
3	300	0,000644	643,5681	0,627412442	0,372588	37,25876
4	400	0,000483	482,6761	0,537119396	0,462881	46,28806
5	500	0,000386	386,1408	0,459820728	0,540179	54,01793
6	600	0,000322	321,784	0,393646372	0,606354	60,63536
7	700	0,000276	275,8149	0,336995392	0,663005	66,30046
8	800	0,000241	241,338	0,288497246	0,711503	71,15028
9	900	0,000215	214,5227	0,246978632	0,753021	75,30214
10	1000	0,000193	193,0704	0,211435102	0,788565	78,85649

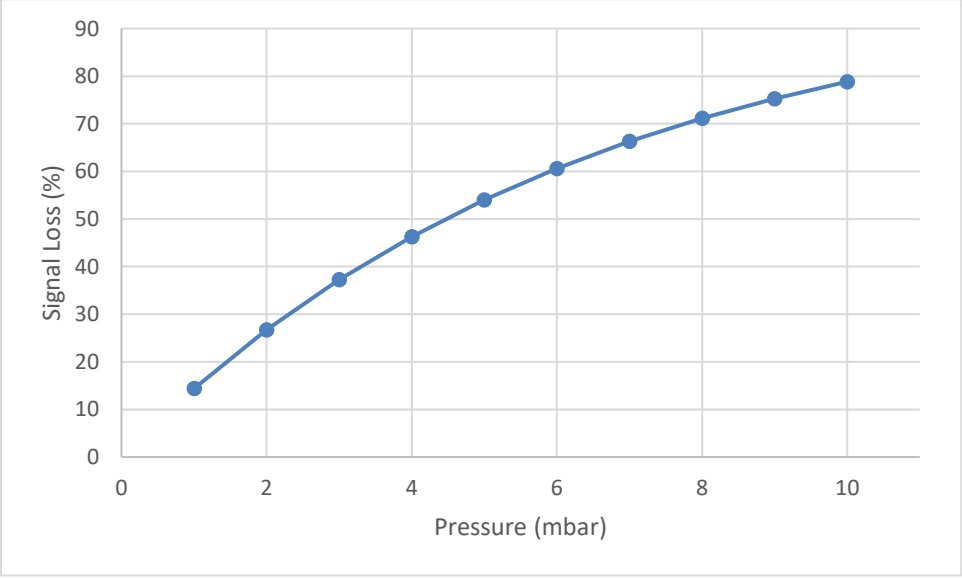

Figure 38 : Signal lost as a Function of pressure in N2 for 1000 eV electrons

Cu In XPS

Copper exhibits multiple transitions in XPS, spanning a wide range of binding energies. It also displays several Auger peaks, with the most prominent being the Cu $L_3M_{4,5}M_{4,5}$ transition. Table 1 summarizes key copper transitions observed in XPS.

Table 4 : Cu main transition visible in XPS in Binding energy

	Cu 2s	Cu $2p_{1/2}$	Cu $2p_{3/2}$	Cu LMM	Cu 3s	Cu 3p
E_B (eV)	1098	953	933	570	123	77

AdC desorption under Ar

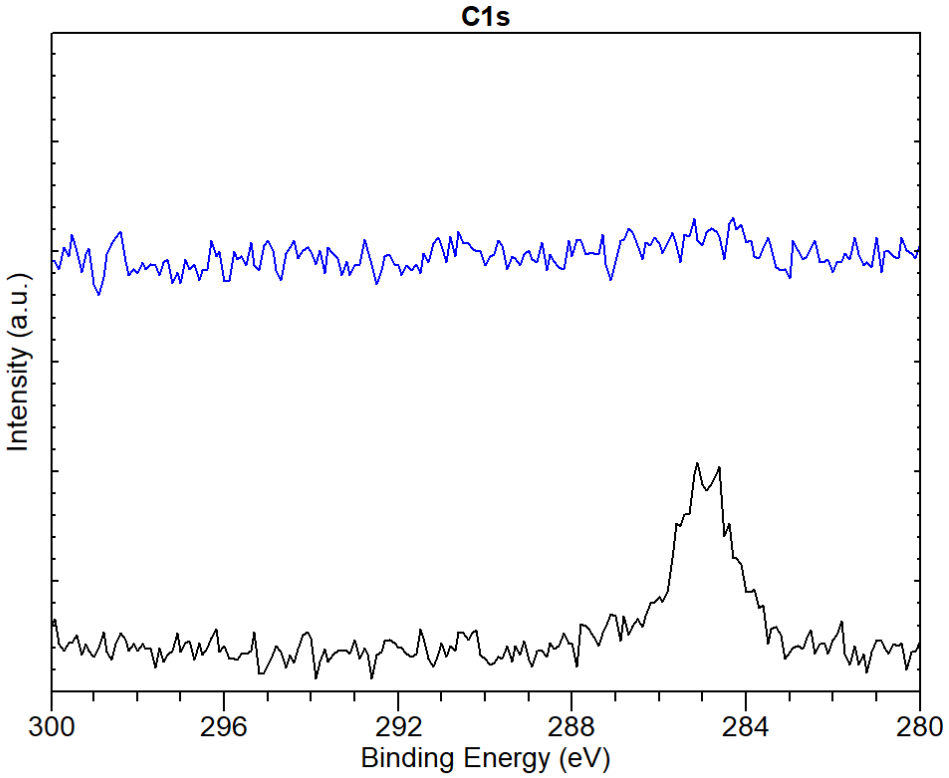

Figure 39 : C 1s spetcrum of a copper plate when heating under Ar 2mbar at 500K

Attempt to reduce the thin oxide layer on the Copper plate

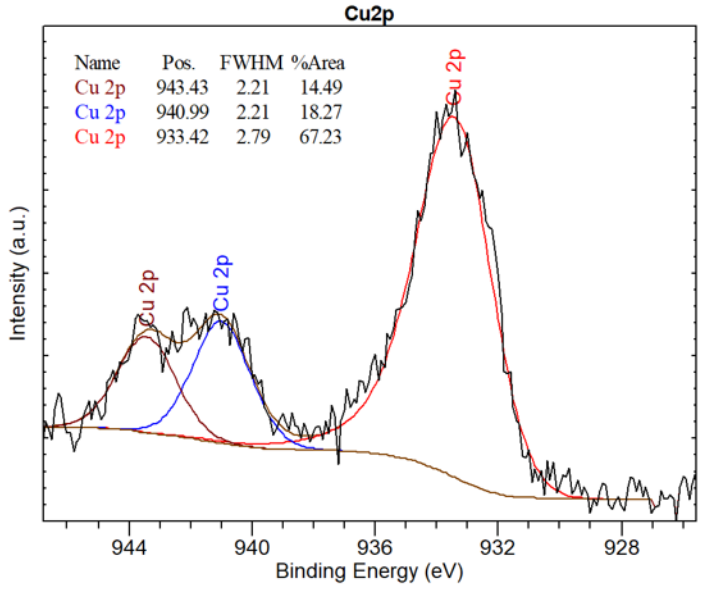

Figure 40 : Cu 2p spectra after succcesive heating under 2 mbar of O2 and then 2 mbar Ar/H2 5%.at 600K

Total cross section for electron in O_2

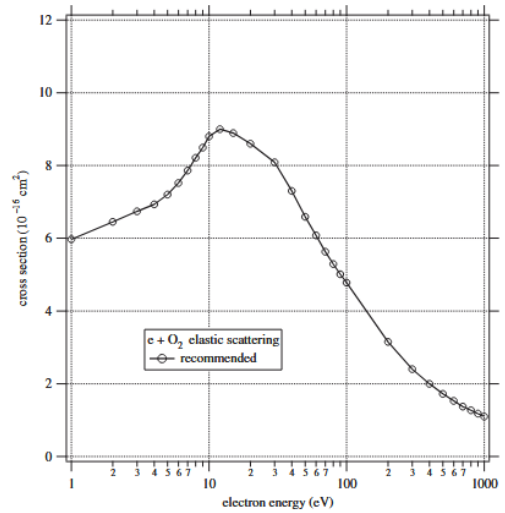

Figure 41 : Total cross section of electron in O_2[31].

Signal attenuation

Table 5 : Data for signal attenuation at 2 mbar

	C 1s	O 1s	Cu 2p
Eb	284,8	532	932
Ek eV	1201,9	954,7	554,7
UHV	7786,2	13492,6	51498
Ar/H2	3736,4	5706,6	16349,4
Ratio	0,479875	0,422943	0,317476
Signal perdu	0,520125	0,577057	0,682524
UHV	7204,4	7438,1	21268,5
O2	3292,7	3694,8	8256,6
Ratio	0,45704	0,49674	0,388208
Signal perdu	0,54296	0,50326	0,611792
UHV	3199,8	3683,1	16396
Ar	1414	1535,2	4471,1
Ratio	0,441903	0,416823	0,272695
Signal perdu	0,558097	0,583177	0,727305
UHV	4312,4	6953,8	33031,9
Air	1810	2941,2	8959,9
Ratio	0,41972	0,422963	0,27125
Signal perdu	0,58028	0,577037	0,72875

Pressure Drop with the Mo plate.

Estimation T2	I2	I1	I1/I2	LnI1/2	P1/T1	Facteur Correction	P2 (Pa)
373	1215,2	659,4	0,542627	-0,61133	3,355704698	2,15962441	759,2242

Ratio Cu 3p/Si 2p

Table 6 : Cu 3p/Si 2p area ratio at different current

	Area (Counts/s)		
	Si 2p	Cu 3p	Cu/Si
RT (SSI)	29323,9	4196,5	0,143109
0.5 A	8447,4	4369,9	0,517307
0.6 A	8022,8	4998,9	0,623087
0.7 A	7579	6171,6	0,814303
0.8 A	7188	6052	0,841959

Cu/SiO2 Catalyst SSI spectra

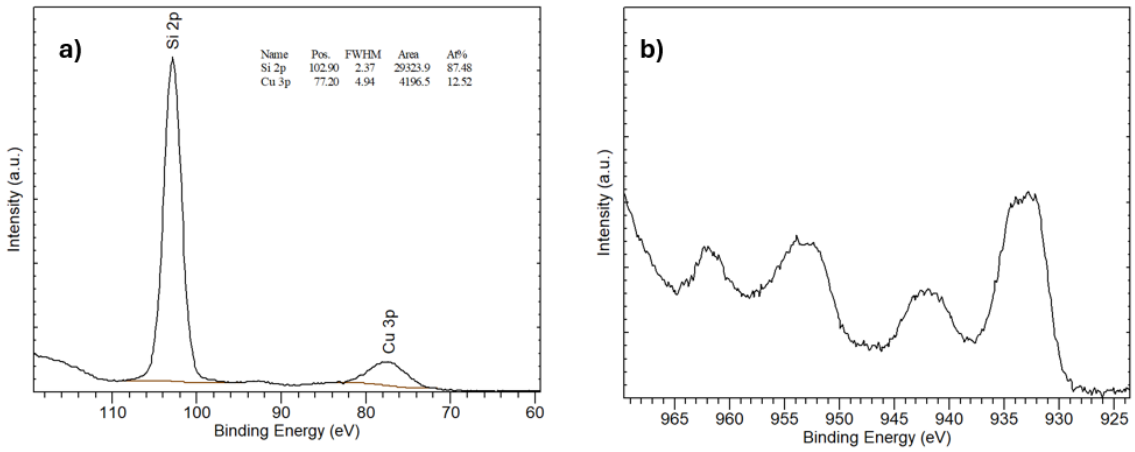

Figure 42 : a) Si 2p + Cu 3p of the catalyst take on the SSI UHV-XPS at room temperature, b) Cu 2p region take on the SSI UHV-XPS at room temperature.

Cu 2p region after migration under heating

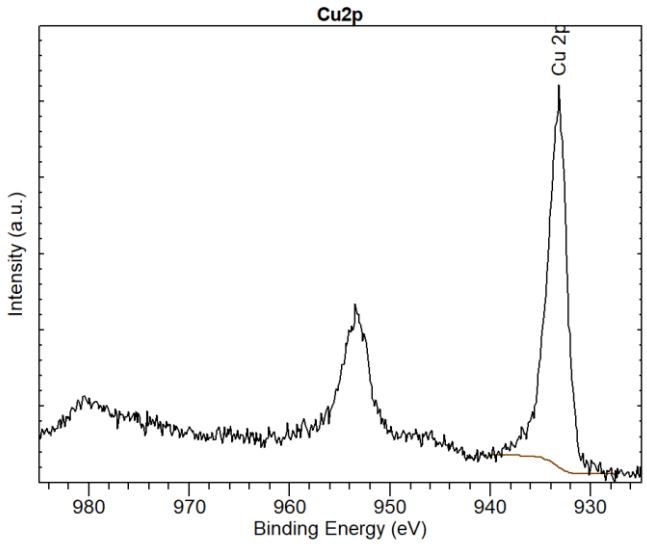

Figure 43: Cu 2p region after migration when heating under UHV

Bibliography

(1) Somorjai, G. A.; Li, Y. *Introduction to Surface Chemistry and Catalysis*; John Wiley & Sons, 2010.
(2) Kumar, R. *Surface Characterization Techniques: From Theory to Research*; De Gruyter, 2022. https://doi.org/10.1515/9783110656480.
(3) Pampararo, G.; Garbarino, G.; Riani, P.; Vykoukal, V.; Busca, G.; Debecker, D. P. Ethanol Dehydrogenation to Acetaldehyde with Mesoporous Cu-SiO2 Catalysts Prepared by Aerosol-Assisted Sol–Gel. *Chem. Eng. J.* **2023**, *465*, 142715. https://doi.org/10.1016/j.cej.2023.142715.
(4) Baer, D. R.; Sherwood, P. M. A. Perspective on the Development of XPS and the Pioneers Who Made It Possible. *Front. Anal. Sci.* **2025**, *4*, 1509438. https://doi.org/10.3389/frans.2024.1509438.
(5) Wheaton, B. R. Photoelectric Effect. In *Compendium of Quantum Physics*; Greenberger, D., Hentschel, K., Weinert, F., Eds.; Springer: Berlin, Heidelberg, 2009; pp 472–475. https://doi.org/10.1007/978-3-540-70626-7_143.
(6) Dupont-Gillain, C. XPS ANALYSIS OF BIOSYSTEMS AND BIOMATERIALS, 2007.
(7) Steinhardt, R.; Serfass, E. X-Ray Photoelectron Spectrometer for Chemical Analysis. *Anal. Chem.* **1951**, *23* (11), 1585–1590. https://doi.org/10.1021/ac60059a019.
(8) Siegbahn, K. Electron Spectroscopy for Atoms, Molecules and Condensed Matter - an Overview. *J. Electron Spectrosc. Relat. Phenom.* **1985**, *36* (2), 113–129. https://doi.org/10.1016/0368-2048(85)80013-X.
(9) Stevie, F. A.; Donley, C. L. Introduction to X-Ray Photoelectron Spectroscopy. *J. Vac. Sci. Technol. Vac. Surf. Films* **2020**, *38* (6), 063204. https://doi.org/10.1116/6.0000412.
(10) Stevens, J. S.; Schroeder, S. L. M. X-Ray Photoelectron Spectroscopy. In *Encyclopedia of Physical Organic Chemistry*; John Wiley & Sons, Ltd, 2017; pp 1–53. https://doi.org/10.1002/9781118468586.epoc4031.
(11) Stojilovic, N. Why Can't We See Hydrogen in X-Ray Photoelectron Spectroscopy? *J. Chem. Educ.* **2012**, *89* (10), 1331–1332. https://doi.org/10.1021/ed300057j.
(12) Moulder, J. F. *Handbook of X-Ray Photoelectron Spectroscopy: A Reference Book of Standard Spectra for Identification and Interpretation of XPS Data*; Physical Electronics Division, Perkin-Elmer Corporation, 1992.
(13) Huttel, Y.; Schiller, F.; Avila, J.; Asensio, M. Electronic and Structural Properties of Mn/Cu Superstructure. *Phys. Rev. B* **2000**, *61*, 4948. https://doi.org/10.1103/PhysRevB.61.4948.
(14) Holloway, P. H. Fundamentals and Applications of Auger Electron Spectroscopy. In *Advances in Electronics and Electron Physics*; Marton, L., Marton, C., Eds.; Academic Press, 1980; Vol. 54, pp 241–298. https://doi.org/10.1016/S0065-2539(08)60100-6.
(15) Mathieu, H. J. Auger Electron Spectroscopy. In *Surface Analysis – The Principal Techniques*; John Wiley & Sons, Ltd, 2009; pp 9–45. https://doi.org/10.1002/9780470721582.ch2.
(16) Biesinger, M. C. Advanced Analysis of Copper X-ray Photoelectron Spectra. *Surf. Interface Anal.* **2017**, *49* (13), 1325–1334. https://doi.org/10.1002/sia.6239.
(17) Grey, L. H.; Nie, H.-Y.; Biesinger, M. C. Defining the Nature of Adventitious Carbon and Improving Its Merit as a Charge Correction Reference for XPS. *Appl. Surf. Sci.* **2024**, *653*, 159319. https://doi.org/10.1016/j.apsusc.2024.159319.
(18) Biesinger, M. C. Accessing the Robustness of Adventitious Carbon for Charge Referencing (Correction) Purposes in XPS Analysis: Insights from a Multi-User Facility Data Review. *Appl. Surf. Sci.* **2022**, *597*, 153681. https://doi.org/10.1016/j.apsusc.2022.153681.
(19) Mayer, B.; Uhlenbrock, St.; Neumann, M. XPS Satellites in Transition Metal Oxides. *J. Electron Spectrosc. Relat. Phenom.* **1996**, *81* (1), 63–67. https://doi.org/10.1016/0368-2048(96)03030-7.

(20) Mosaferi, M.; Selles, P.; Miteva, T.; Ferté, A.; Carniato, S. Interpretation of Shakeup Mechanisms in Copper L-Shell Photoelectron Spectra. *J. Phys. Chem. A* **2022**, *126* (30), 4902–4914. https://doi.org/10.1021/acs.jpca.2c01870.
(21) Jablonski, A.; Powell, C. J. Relationships between Electron Inelastic Mean Free Paths, Effective Attenuation Lengths, and Mean Escape Depths. *J. Electron Spectrosc. Relat. Phenom.* **1999**, *100* (1), 137–160. https://doi.org/10.1016/S0368-2048(99)00044-4.
(22) Powell, C. J. Practical Guide for Inelastic Mean Free Paths, Effective Attenuation Lengths, Mean Escape Depths, and Information Depths in x-Ray Photoelectron Spectroscopy. *J. Vac. Sci. Technol. A* **2020**, *38* (2), 023209. https://doi.org/10.1116/1.5141079.
(23) Lesiak, B.; Jablonski, A.; Zemek, J.; Jiricek, P. Determination of the Inelastic Mean Free Paths of Electrons in Copper and Copper Oxides by Elastic Peak Electron Spectroscopy (EPES). *Surf. Interface Anal.* **1998**, *26* (5), 400–411. https://doi.org/10.1002/(SICI)1096-9918(19980501)26:5<400::AID-SIA385>3.0.CO;2-0.
(24) Tao, F. (Feng); Nguyen, L. Interactions of Gaseous Molecules with X-Ray Photons and Photoelectrons in AP-XPS Study of Solid Surface in Gas Phase. *Phys. Chem. Chem. Phys.* **2018**, *20* (15), 9812–9823. https://doi.org/10.1039/C7CP08429C.
(25) Itikawa, Y. Cross Sections for Electron Collisions with Nitrogen Molecules. *J. Phys. Chem. Ref. Data* **2005**, *35* (1), 31–53. https://doi.org/10.1063/1.1937426.
(26) Salmeron, M.; Schlogl, R. Ambient Pressure Photoelectron Spectroscopy: A New Tool for Surface Science and Nanotechnology. *Surf. Sci. Rep.* **2008**, *63* (4), 169–199. https://doi.org/10.1016/j.surfrep.2008.01.001.
(27) Siol, S.; Mann, J.; Newman, J.; Miyayama, T.; Watanabe, K.; Schmutz, P.; Cancellieri, C.; Jeurgens, L. P. H. Advanced Chemical State Studies of Oxide Films by Lab-Based HAXPES Combining Soft and Hard X-Ray Sources. *Surf. Interface Anal.* **2020**, *52* (12), 802–810. https://doi.org/10.1002/sia.6790.
(28) Carenco, S.; Sassoye, C.; Faustini, M.; Eloy, P.; Debecker, D. P.; Bluhm, H.; Salmeron, M. The Active State of Supported Ruthenium Oxide Nanoparticles during Carbon Dioxide Methanation. *J. Phys. Chem. C* **2016**, *120* (28), 15354–15361. https://doi.org/10.1021/acs.jpcc.6b06313.
(29) Arble, C.; Jia, M.; Newberg, J. T. Lab-Based Ambient Pressure X-Ray Photoelectron Spectroscopy from Past to Present. *Surf. Sci. Rep.* **2018**, *73* (2), 37–57. https://doi.org/10.1016/j.surfrep.2018.02.002.
(30) Starr, D. E. A Brief Overview of the Principles of Ambient Pressure X-Ray Spectroscopies. In *Ambient Pressure Spectroscopy in Complex Chemical Environments*; ACS Symposium Series; American Chemical Society, 2021; Vol. 1396, pp 1–17. https://doi.org/10.1021/bk-2021-1396.ch001.
(31) Itikawa, Y. Cross Sections for Electron Collisions with Oxygen Molecules. *J. Phys. Chem. Ref. Data* **2008**, *38* (1), 1–20. https://doi.org/10.1063/1.3025886.
(32) Pielsticker, L.; Nicholls, R.; Beeg, S.; Hartwig, C.; Klihm, G.; Schlögl, R.; Tougaard, S.; Greiner, M. Inelastic Electron Scattering by the Gas Phase in near Ambient Pressure XPS Measurements. *Surf. Interface Anal.* **2021**, *53* (7), 605–617. https://doi.org/10.1002/sia.6947.
(33) Jürgensen, A.; Esser, N.; Hergenröder, R. Near Ambient Pressure XPS with a Conventional X-Ray Source. *Surf. Interface Anal.* **2012**, *44* (8), 1100–1103. https://doi.org/10.1002/sia.4826.
(34) Kahk, J. M.; Villar-Garcia, I. J.; Grechy, L.; Bruce, P. J. K.; Vincent, P. E.; Eriksson, S. K.; Rensmo, H.; Hahlin, M.; Åhlund, J.; Edwards, M. O. M.; Payne, D. J. A Study of the Pressure Profiles near the First Pumping Aperture in a High Pressure Photoelectron Spectrometer. *J. Electron Spectrosc. Relat. Phenom.* **2015**, *205*, 57–65. https://doi.org/10.1016/j.elspec.2015.08.005.
(35) Li, H.; Jana, A.; Garcia-Esparza, A. T.; Li, X.; Kaminsky, C. J.; Hamlyn, R.; Prabhakar, R. R.; Atwater, H. A.; Ager, J. W.; Sokaras, D.; Yano, J.; Crumlin, E. J. When Photoelectrons Meet Gas Molecules: Determining the Role of Inelastic Scattering in Ambient Pressure X-Ray Photoelectron Spectroscopy. *ACS Cent. Sci.* **2025**, *11* (1), 98–106. https://doi.org/10.1021/acscentsci.4c01841.
(36) Debecker, D. P. Innovative Sol-Gel Routes for the Bottom-Up Preparation of Heterogeneous Catalysts. *Chem. Rec.* **2018**, *18* (7–8), 662–675. https://doi.org/10.1002/tcr.201700068.

(37) Debecker, D. P.; Bras, S. L.; Boissière, C.; Chaumonnot, A.; Sanchez, C. Aerosol Processing: A Wind of Innovation in the Field of Advanced Heterogeneous Catalysts. *Chem. Soc. Rev.* **2018**, *47* (11), 4112–4155. https://doi.org/10.1039/C7CS00697G.
(38) Garbarino, G.; Pampararo, G.; Phung, T. K.; Riani, P.; Busca, G. Heterogeneous Catalysis in (Bio)Ethanol Conversion to Chemicals and Fuels: Thermodynamics, Catalysis, Reaction Paths, Mechanisms and Product Selectivities. *Energies* **2020**, *13* (14), 3587. https://doi.org/10.3390/en13143587.
(39) Nguyen, L.; Tao, F. F.; Tang, Y.; Dou, J.; Bao, X.-J. Understanding Catalyst Surfaces during Catalysis through Near Ambient Pressure X-Ray Photoelectron Spectroscopy. *Chem. Rev.* **2019**, *119* (12), 6822–6905. https://doi.org/10.1021/acs.chemrev.8b00114.
(40) Li, M.; Pham, T. H. M.; Oveisi, E.; Ko, Y.; Luo, W.; Züttel, A. Revealing the Surface Chemistry for CO2 Hydrogenation on Cu/CeO2–x Using Near-Ambient-Pressure X-Ray Photoelectron Spectroscopy. *ACS Appl. Energy Mater.* **2021**, *4* (11), 12326–12335. https://doi.org/10.1021/acsaem.1c02146.
(41) Leonzio, G.; Zondervan, E.; Foscolo, P. U. Methanol Production by CO2 Hydrogenation: Analysis and Simulation of Reactor Performance. *Int. J. Hydrog. Energy* **2019**, *44* (16), 7915–7933. https://doi.org/10.1016/j.ijhydene.2019.02.056.
(42) López-Rodríguez, S.; Davó-Quiñonero, A.; Bailón-García, E.; Lozano-Castelló, D.; Villar-Garcia, I. J.; Dieste, V. P.; Calvo, J. A. O.; Velasco, J. R. G.; Bueno-López, A. Monitoring by in Situ NAP-XPS of Active Sites for CO2 Methanation on a Ni/CeO2 Catalyst. *J. CO2 Util.* **2022**, *60*, 101980. https://doi.org/10.1016/j.jcou.2022.101980.
(43) Bluhm, H.; Hävecker, M.; Knop-Gericke, A.; Kleimenov, E.; Schlögl, R.; Teschner, D.; Bukhtiyarov, V. I.; Ogletree, D. F.; Salmeron, M. Methanol Oxidation on a Copper Catalyst Investigated Using in Situ X-Ray Photoelectron Spectroscopy. *J. Phys. Chem. B* **2004**, *108* (38), 14340–14347. https://doi.org/10.1021/jp040080j.
(44) Haug, L.; Griesser, C.; Thurner, C. W.; Winkler, D.; Moser, T.; Thaler, M.; Bartl, P.; Rainer, M.; Portenkirchner, E.; Schumacher, D.; Dierschke, K.; Köpfle, N.; Penner, S.; Beyer, M. K.; Loerting, T.; Kunze-Liebhäuser, J.; Klötzer, B. A Laboratory-Based Multifunctional near Ambient Pressure X-Ray Photoelectron Spectroscopy System for Electrochemical, Catalytic, and Cryogenic Studies. *Rev. Sci. Instrum.* **2023**, *94* (6), 065104. https://doi.org/10.1063/5.0151755.
(45) Grant, J. T. Challenges in Surface Analysis. *Front. Anal. Sci.* **2023**, *3*. https://doi.org/10.3389/frans.2023.1234943.
(46) Ogletree, D. F.; Bluhm, H.; Lebedev, G.; Fadley, C. S.; Hussain, Z.; Salmeron, M. A Differentially Pumped Electrostatic Lens System for Photoemission Studies in the Millibar Range. *Rev. Sci. Instrum.* **2002**, *73* (11), 3872–3877. https://doi.org/10.1063/1.1512336.
(47) Markevich, N.; Gertner, I. Comparison among Methods for Calculating FWHM. *Nucl. Instrum. Methods Phys. Res. Sect. Accel. Spectrometers Detect. Assoc. Equip.* **1989**, *283* (1), 72–77. https://doi.org/10.1016/0168-9002(89)91258-8.
(48) Biesinger, M. C.; Lau, L. W. M.; Gerson, A. R.; Smart, R. St. C. Resolving Surface Chemical States in XPS Analysis of First Row Transition Metals, Oxides and Hydroxides: Sc, Ti, V, Cu and Zn. *Appl. Surf. Sci.* **2010**, *257* (3), 887–898. https://doi.org/10.1016/j.apsusc.2010.07.086.
(49) Henderson, J. D.; Payne, B. P.; McIntyre, N. S.; Biesinger, M. C. Enhancing Oxygen Spectra Interpretation by Calculating Oxygen Linked to Adventitious Carbon. *Surf. Interface Anal.* **2025**, *57* (3), 214–220. https://doi.org/10.1002/sia.7376.
(50) Greczynski, G. Binding Energy Referencing in X-Ray Photoelectron Spectroscopy: Expanded Data Set Confirms That Adventitious Carbon Aligns to the Vacuum Level. *Appl. Surf. Sci.* **2024**, *670*, 160666. https://doi.org/10.1016/j.apsusc.2024.160666.
(51) Biesinger, M. C. Accessing the Robustness of Adventitious Carbon for Charge Referencing (Correction) Purposes in XPS Analysis: Insights from a Multi-User Facility Data Review. *Appl. Surf. Sci.* **2022**, *597*, 153681. https://doi.org/10.1016/j.apsusc.2022.153681.

(52) Patel, D. I.; Bahr, S.; Dietrich, P.; Meyer, M.; Thißen, A.; Linford, M. R. Ambient Air, by near-Ambient Pressure XPS. *Surf. Sci. Spectra* **2019**, *26* (2), 024002. https://doi.org/10.1116/1.5099497.
(53) Choudhary, S.; Sarma, J. V. N.; Pande, S.; Ababou-Girard, S.; Turban, P.; Lepine, B.; Gangopadhyay, S. Oxidation Mechanism of Thin Cu Films: A Gateway towards the Formation of Single Oxide Phase. *AIP Adv.* **2018**, *8* (5), 055114. https://doi.org/10.1063/1.5028407.
(54) Avval, T. G.; Chatterjee, S.; Bahr, S.; Dietrich, P.; Meyer, M.; Thißen, A.; Linford, M. R. Carbon Dioxide Gas, CO2(g), by near-Ambient Pressure XPS. *Surf. Sci. Spectra* **2019**, *26* (1), 014022. https://doi.org/10.1116/1.5053761.
(55) Rahmani Didar, B.; Balbuena, P. B. Adsorption of Carbon on Partially Oxidized Low-Index Cu Surfaces. *Langmuir* **2018**, *34* (4), 1311–1320. https://doi.org/10.1021/acs.langmuir.7b03456.
(56) Unutulmazsoy, Y.; Cancellieri, C.; Chiodi, M.; Siol, S.; Lin, L.; Jeurgens, L. P. H. In Situ Oxidation Studies of Cu Thin Films: Growth Kinetics and Oxide Phase Evolution. *J. Appl. Phys.* **2020**, *127* (6), 065101. https://doi.org/10.1063/1.5131516.
(57) Jablonski, A.; Powell, C. J. Effective Attenuation Lengths for Different Quantitative Applications of X-Ray Photoelectron Spectroscopy. *J. Phys. Chem. Ref. Data* **2020**, *49* (3), 033102. https://doi.org/10.1063/5.0008576.
(58) Tao, F. (Feng); Nguyen, L. Interactions of Gaseous Molecules with X-Ray Photons and Photoelectrons in AP-XPS Study of Solid Surface in Gas Phase. *Phys. Chem. Chem. Phys.* **2018**, *20* (15), 9812–9823. https://doi.org/10.1039/C7CP08429C.
(59) SPECS Surface Nano Analysis GmbH. Photoelectron Attenuation Correction for Quantitative NAP XPS, 2023. https://www.specs-group.com/fileadmin/user_upload/applications/Application_Note_NAP_XPS_Quantification_PTFE_final.pdf.
(60) Arcos, T. de los; Müller, H.; Weinberger, C.; Grundmeier, G. UV-Enhanced Environmental Charge Compensation in near Ambient Pressure XPS. *J. Electron Spectrosc. Relat. Phenom.* **2023**, *264*, 147317. https://doi.org/10.1016/j.elspec.2023.147317.
(61) Jensen, D. S.; Kanyal, S. S.; Madaan, N.; Vail, M. A.; Dadson, A. E.; Engelhard, M. H.; Linford, M. R. Silicon (100)/SiO2 by XPS. *Surf. Sci. Spectra* **2013**, *20* (1), 36–42. https://doi.org/10.1116/11.20121101.
(62) Ferry, D. K.; Rode, D. L. Physical and Electrical Properties of Silica. *Appl. Phys. Rev.* **2025**, *12* (1), 011304. https://doi.org/10.1063/5.0233576.
(63) Amano, F.; Tanaka, T.; Funabiki, T. Auto-Reduction of Cu(II) Species Supported on Al2O3 to Cu(I) by Thermovacuum Treatment. *J. Mol. Catal. Chem.* **2004**, *221* (1), 89–95. https://doi.org/10.1016/j.molcata.2004.06.014.
(64) Influence of Ion Mobility on the Redox and Catalytic Properties of Cu Ions in Zeolites. *Chem. Sci.* **2022**, *13* (35), 10238–10250. https://doi.org/10.1039/d2sc03565k.
(65) Millan, R.; Cnudde, P.; van Speybroeck, V.; Boronat, M. Mobility and Reactivity of Cu+ Species in Cu-CHA Catalysts under NH3-SCR-NOx Reaction Conditions: Insights from AIMD Simulations. *JACS Au* **2021**, *1* (10), 1778–1787. https://doi.org/10.1021/jacsau.1c00337.
(66) Soorani, M.; Mele, E.; Christie, J. K. Structural Effects of Incorporating Cu+ and Cu2+ Ions into Silicate Bioactive Glasses Using Molecular Dynamics Simulations. *Mater. Adv.* **2023**, *4* (9), 2078–2087. https://doi.org/10.1039/D2MA00872F.

NAP-XPS analysis in a heterogeneous catalysis context

Presented By Sacha Duriau

Since catalytic reactions in heterogeneous catalysis occur at the surface, understanding surface structure and composition is essential. Near-Ambient Pressure X-ray Photoelectron Spectroscopy is a powerful technique that enables the investigation of catalytic surfaces under conditions close to those of real operation. This master's thesis presents an initial study using the newly installed NAP-XPS system at UCLouvain. As a preliminary step, a pure copper plate was analyzed under various gas atmospheres and temperatures. This allowed us to evaluate the performance of the system and to better understand key instrumental parameters. Additionally, we aimed to evaluate the extent of electron loss occurring in the gas phase. In a second time mesoporous Cu/SiO_2 catalyst was studied to explore the migration of copper species to the surface during calcination. Although this objective was not fully achieved, this work provided valuable insights into gas-phase charge compensation, fluidic effect under the cone, and factors influencing signal attenuation from gas-phase.

UNIVERSITÉ CATHOLIQUE DE LOUVAIN
Faculté des bioingénieurs
Croix du Sud, 2 bte L7.05.01, 1348 Louvain-la-Neuve, Belgique | **www.uclouvain.be/agro**